Present-day deformations of the Jura arc inferred by GPS surveying and earthquake focal mechanisms

Mickael Rabin, Christian Sue, Andrea Walpersdorf, Pierre Sakic, Julie Albaric, Benjamin Fores

AGU100 ADVANCING EARTH AND SPACE SCIENCE

Tectonics

RESEARCH ARTICLE
10.1029/2018TC005047

Special Section:
Geodynamics, Crustal and Lithospheric Tectonics, and active deformation in the Mediterranean Regions (A tribute to Prof. Renato Funiciello)

Present-Day Deformations of the Jura Arc Inferred by GPS Surveying and Earthquake Focal Mechanisms

Mickael Rabin[1], Christian Sue[1], Andrea Walpersdorf[2], Pierre Sakic[3], Julie Albaric[1], and Benjamin Fores[1]

[1]UBFC, CNRS UMR 6249, OSU THETA, Besançon, France, [2]CNRS, IRD, IFSTTAR, ISTerre, Université Grenoble Alpes, Université Savoie Mont Blanc, Grenoble, France, [3]Helmholtz Centre Potsdam, Space Geodetic Techniques Section, GFZ German Research Centre for Geosciences, Potsdam, Germany

Abstract This study presents a compilation of more than 40 years of seismotectonic data, including 54 computed focal mechanisms, combined with 15 years of GPS data coming from a dense network of 35 permanent GPS stations within the Jura arc and its vicinity. These data are compared to previous available geomorphological, geophysical, and structural studies in order to discuss the 3D distribution of the deformation within the Jura arc. GPS data show coherent schemes in terms of velocities and allowed to discriminate between two provinces (NE of the belt and in its front/foreland). They also constrain a low but significant overall strain tensor with a NNW-SSE shortening of 2.16 nanostrain/year associated with an ENE-WSW extension of 0.44 nanostrain/year. The seismotectonic approach is based on a data set of 2,400 events and 54 focal mechanisms. Inversions of the focal mechanisms both globally and in homogeneous sectors highlight a general strike-slip deformation regime, with sigma1 oriented NW-SE and sigma3 oriented NE-SW. We discriminate two different sectors in terms of basement/cover (un)coupling: (1) potentially decoupled deformation between the basement and the sedimentary cover in the NE part; and (2) coupled deformation in the sedimentary cover and its basement in the Jura foreland.

Key Points:
- Coupled sismotectonic-geodesic study of the Jura arc (northwestern most part of the Alps)
- Decoupling between basement and sedimentary cover in the northeastern part
- Good coherency between GPS and seismotectonics results

Correspondence to:
C. Sue,
csue@univ-fcomte.fr

Citation:
Rabin, M., Sue, C., Walpersdorf, A., Sakic, P., Albaric, J., & Fores, B. (2018). Present-day deformations of the Jura arc inferred by GPS surveying and earthquake focal mechanisms. *Tectonics*, *37*, 3782–3804. https://doi.org/10.1029/2018TC005047

Received 7 MAR 2018
Accepted 12 SEP 2018
Accepted article online 28 SEP 2018
Published online 18 OCT 2018

1. Introduction

The Jura Mountains represent the northwesternmost extension of the European Alps (Sue & Schmid, 2017). This typical thrust-and-fold belt is one of the best studied orogenic arcs in the world (e.g., Aubert, 1949; Becker, 2000; Burkhard, 1990; Heim, 1919; Henry et al., 1997; Laubscher, 2010; Lebeau, 1951; Lyon-Caen & Molnar, 1989; Pfiffner, 1990; Rollier, 1903; Schlunegger et al., 1997; Sommaruga, 1999). However, its neotectonic activity remains a matter of debates, and several structural and tectonic models have been proposed from ongoing thin-skinned compression to thick-skinned deformation and from compression to transpression or even arc-parallel extension. In this study, we combine available GPS data from permanent GPS networks, including the recently installed GPS-JURA network, with available seismological data (focal mechanisms and earthquake catalogs) in the vicinity of the belt in order to characterize the ongoing tectonics in the surrounding of the Jura Mountain. Based on our new data set, we discuss the 3D distribution of the deformation and the ongoing dynamics. In the following we distinguish the thick-skinned deformation model as defined by Coward (1983) implying that the compression is accommodated by steep thrusts affecting the overall fragile crust from the involvement of the basement only in strike-slip faulting, without a shortening component. Given that point, we discuss the regionalization of the thin-skin versus thick-skin deformation around the bend of the Jura arc.

2. Geological Setting

The Jura Mountains are the most external and one of the most recent tectonic expressions of the Alpine orogeny (Figure 1). Its orogeny took place between 9 and 3.3 Ma (Becker, 2000, and references therein) and corresponds to a fold-and-thrust belt with an arc-shape northward of the western Alpine Foreland. Its southern tip merges with the front of the subalpine belt, while its northeastern part is separated from the Alps by the Molasse Basin. This Oligo-Miocene foredeep basin developed at the northern front of the European Alps (Aubert, 1949; Becker, 2000; Burkhard, 1990; Heim, 1919; Henry et al., 1997; Laubscher, 2010; Lebeau, 1951; Lyon-Caen & Molnar, 1989; Pfiffner, 1990; Rollier, 1903; Schlunegger et al., 1997; Sommaruga, 1999).

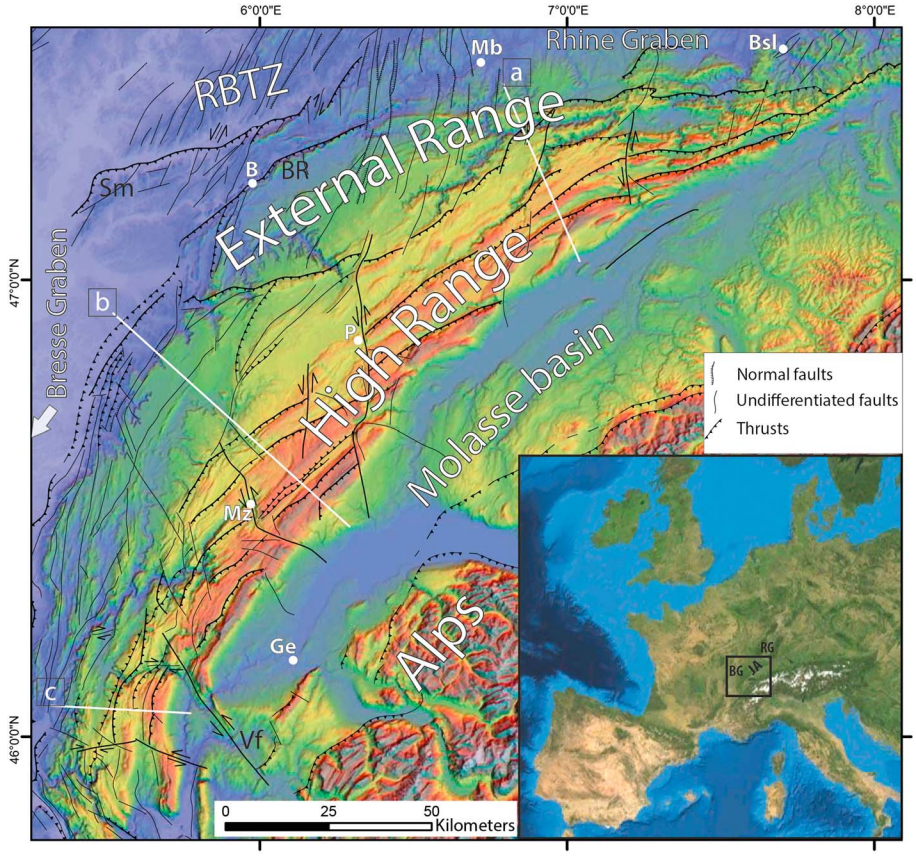

Figure 1. Simplified structural map of the Jura Mountains. Bsl = Basel, B = Besançon, Ge = Geneva, Mb = Montbéliard, Mz = Morez, P = Pontarlier, Sm = Serre massif, BR = Besançon Range, Vf = Vuache fault, RBTZ = Rhine-Bresse transform zone; JA = Jura arc; RG = Rhine graben; BG = Bresse graben. Thrusts are indicated with small triangles on the lines. Other fault types are undifferentiated, except the main traversing left-lateral strike-slip faults. The inset shows the location of the study area within Western Europe.

The Jura Mountains are surrounded to the west and the north by peri-alpine N-S oriented Tertiary rifts (Bresse and Rhine grabens, see Merle and Michon, 2001; Dèzes et al., 2004; Figure 1). Its northern boundary is affected by NNE-SSW to ENE-WSW striking normal faults associated to Tertiary rifting and corresponding to the Rhine-Bresse Transfer Zone (RBTZ; Figure 1; Lacombe et al., 1993, and references therein; Madritsch et al., 2009). The Jura Mountains consist of Mesozoic and Cenozoic deformed marls and limestones that were detached from the underlying Paleozoic basement (Figure 2) on Triassic evaporites located at the base of the folded arc (e.g., Affolter & Gratier, 2004). Meso-Cenozoic sediments are hardly deformed in the Molasse Basin, whereas they acquired a typical fold-and-thrust structure westward in the Jura arc. The Paleozoic basement is exposed beyond the northern front of the Jura (Serre massif; Figure 1) and is composed of medium to high grade metamorphic and plutonic rocks deformed during the Variscan orogeny covered by Stephano-Permian sediments.

The Jura belt is a typical thin-skinned fold-and-thrust belt (Affolter & Gratier, 2004; Becker, 2000; Burkhard & Sommaruga, 1998; Hindle, 1997; Homberg et al., 1999; Laubscher, 1992), composed of narrow strained zones separated by hardly deformed plateaus. These deformed zones, the so-called *Jura Faisceaux*, are affected by arc-parallel folds and thrusts corresponding to a horizontal, SSE-NNW directed shortening. Its overall structure can be resumed in three main regions: (i) the High Range in the internal part (eastward), which is separated from (ii) the External Range to the west by (iii) barely deformed plateaus in the central part (Figure 1).

The fold-and-thrust arcuate structure of the Jura is crosscut by coeval left-lateral transpressive faults (e.g., Vuache, Morez, and Pontarlier faults; e.g., De La Taille, 2015; Figure 1), which delineate individual tectonic blocks and accommodated part of the shortening (Affolter & Gratier, 2004; Becker, 2000; Homberg et al.,

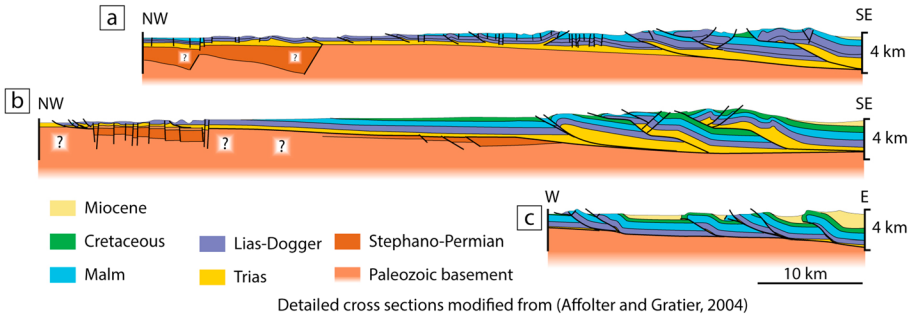

Figure 2. Schematic cross sections (modified after Affolter & Gratier, 2004) approximatively relocated in Figure 1 (white lines). Question marks on cross sections represent uncertainties on the deep geometry of the basement. The three sections are detached in the Trias evoporites (Keuper).

1997; Laubscher, 1992). The northern and eastern parts of the Jura are characterized by E-W to NE-SW trending fold axes and thrusts and N-S striking left-lateral strike-slip faults, whereas in the southwestern part thrusts and fold axes mostly trend N-S and strike-slip faults strike NW-SE (Affolter & Gratier, 2004) (Figure 1).

The typical stair-step shape of the Jura structure was acquired during the latest stage of the Alpine orogeny, in Late Miocene and Early Pliocene times (Affolter & Gratier, 2004; Becker, 2000; Sommaruga, 1999). Folding and thrusting took place between about 14 and 3.3 Ma according to stratigraphic and paleontological evidence (Becker, 2000; Ustaszewski & Schmid, 2006, 2007, and references therein). However, geomorphological evidence suggest that more recent deformation (i.e., Pleistocene to Holocene) occurred along the northernmost frontal thrusts of the Jura (Carretier et al., 2006; Giamboni, Wetzel, et al., 2004; Madritsch, Preusser, et al., 2010; Molliex et al., 2011; Nivière et al., 2006; Nivière & Winter, 2000; Ustaszewski & Schmid, 2006, 2007). These authors highlight Plio-Pleistocene N-S horizontal shortening in the external part of the Jura and uplift with a velocity ranging between 0.05 and 0.2 mm/year at the front (e.g., Giamboni, Wetzel, et al., 2004; Madritsch, Preusser, et al., 2010).

Neotectonic activity of the Jura has been studied using different geophysical and geomorphological approaches (De La Taille, 2015; Giamboni, Wetzel, et al., 2004; Jouanne et al., 1995, 1998; Madritsch, Fabbri, et al., 2010; Madritsch, Preusser, et al., 2010; Nivière & Winter, 2000; Nocquet & Calais, 2003; Vouillamoz, 2015; Walpersdorf et al., 2006). Jouanne et al. (1995, 1998), Nivière and Winter (2000), and Nivière et al. (2006) have proposed a northward propagation of thin-skinned thrusting deformation with uplift rates of ~0.7 mm/year from leveling data in the internal part of the southern Jura (Jouanne et al., 1998; Figure 3b in Jouanne et al., 1998) and a long-term mean uplift velocity of ~0.3 mm/year along the northernmost frontal thrust (Nivière et al., 2006). Horizontal velocities have been estimated by GPS/triangulation methods to 3 to 4 mm/year and associated with an E-W shortening (Jouanne et al., 1998), which appear nowadays much overestimated (e.g., Walpersdorf et al., 2018, this volume). Also, recent geodetic studies based on GPS network analyses have revealed horizontal velocities lower than 1 mm/year (Nocquet & Calais, 2003; Walpersdorf et al., 2006) associated with a main strain feature in favor of an arc-parallel extension. Moreover, geomorphological evidence of fold growth suggests a long-term mean uplift velocity of only ~0.05 mm/year along the External Range, eventually associated with a thick-skinned deformation mode (Giamboni, Wetzel, et al., 2004; Madritsch, Fabbri, et al., 2010; Molliex et al., 2011; Rabin et al., 2015; Ustaszewski & Schmid, 2007).

Considering the hypothesis of ongoing horizontal shortening, there is a debate about both the actual deformation style (thin-skinned versus thick-skinned) and the long-term mean uplift rates (from 0.05 to 0.7 mm/year). The neotectonic activity in the Jura Mountains is also discussed in terms of deformation style based on the seismicity data and focal mechanisms. Indeed, Lacombe and Mouthereau (2002) noted that the majority of earthquakes recorded in the Jura Mountains and their vicinity are distributed throughout the entire crust, down to 30-km depth, with a higher density around 15–20-km depth. The deepest crustal earthquakes have been associated with the presence of high-pressure fluids, which favor brittle failure at such depths (Deichmann, 1992). This seismicity pattern argues for present-day activity in the basement under the Jura cover and has been interpreted as evidence for ongoing shortening in a thick-skinned mode (Lacombe &

Mouthereau, 2002). Nevertheless, the general synthesis of earthquakes occurring in the Jura and the northern Alps proposed by Kastrup et al. (2004) has shown that most earthquakes in the Jura belt have strike-slip focal mechanisms. Moreover, the majority of recorded earthquakes are located in the south part of the Rhine Graben with focal mechanisms associated with WNW-SSE striking steep faults (e.g., Kastrup et al., 2004; Lacombe & Mouthereau, 2002), which is not in agreement with the orientations of the inherited Variscan faults (Affolter & Gratier, 2004 Hindle, 1997; Homberg et al., 2002, and references therein; Ustaszewski & Schmid, 2006). However, the relatively poor resolution of epicentral depth, together with the absence of lower crustal reverse faulting events in the southwestern Jura, and a dominant strike-slip tectonic mode evidenced by focal mechanisms do not support the interpretation of an ongoing thick-skinned activity (as defined by Coward, 1983) generalized in the Jura Mountains.

Beyond the debate on the deformation mode in the Jura arc, the model of an ongoing active collision for the Jura would raise the issue of its geodynamic origin. The Western Alps are in a postcollisional regime (Champagnac et al., 2009; Delacou et al., 2005; Nocquet, 2012; Sue et al., 2002; Sue et al., 2007; Valla et al., 2012) and are characterized by isostatic-related extension in their core partly correlated with an active uplift, due to the interaction between buoyancy forces and erosional dynamics (Baran et al., 2014; Champagnac et al., 2007; Delacou et al., 2008; Nocquet et al., 2016; Serpelloni et al., 2013; Sue et al., 1999; Sue & Tricart, 2003; Sue et al., 2007; Tricart et al., 2006; Vernant et al., 2013).

In this study, we compare the stress field directions obtained by inverting more than 50 focal mechanisms distributed along the entire arc with the strain rates obtained from GPS data recorded since 2000 in the vicinity of the Jura Mountains in order to better constrain its current deformation.

3. Seismotectonic Analysis

3.1. Seismological Setting

Figure 3 represents the seismicity of the Jura Mountain between 1971 and 2012 recorded by the French Alpine Seismic Network, the French National Seismic Monitoring Network, and the Swiss Seismological Service (SED). The station locations of these three networks around the Jura Mountains are presented on Figure 4. The seismic activity is continuous through the observation period with more than 2,400 events distributed over the entire arc with a maximum magnitude of 5.2. In the northeastern part of the Jura Mountains, both the External Range and the High Range present moderate seismic activity (Figure 3). The northeastern most part of this area is affected by some normal faulting at the southern termination of the Rhine Graben, although strike-slip remains the dominant mode. In the southwest of the Jura arc a cluster of moderate to large earthquakes, with M_l from 3 to 5.3 (1996 Epagny earthquake sequence; Thouvenot et al., 1998), is located at the southern tip of the Vuache fault (A mark on Figure 3). Smaller earthquakes ($M_l < 3$) occur farther north along this left lateral strike-slip fault highlighting its ongoing seismic activity (Figure 1 and 3). The Vuache fault's seismicity occurs in the sedimentary cover (Thouvenot et al., 1998).

The majority of the earthquakes have local magnitudes lower or equal to 3 (more than 2,300 events). Only six events have a magnitude higher than 4 in the period 1971–2012. The three biggest events were the M_l 5.2–5.3 Vuache earthquake in 1996 (Thouvenot et al., 1998), the M_l 4.8–5.1 Besançon earthquake in 2004 (Baer et al., 2005), and the M_l 4.7–4.8 Sierentz earthquake in 1980 (Maury et al., 2013; Rouland et al., 1980), respectively, A, B and C on Figure 3.

An average of 20 to 30 events with $M_l \leq 3$ and less than three events with higher magnitudes occur each year in the Jura Mountains (Figure 5c). The seismic events are distributed in depth up to 35 km with a peak between 5 and 15 km (Figure 5b). Vertical earthquake locations are poorly constrained with uncertainties reaching up to 10 km or more due to the sparse seismic network coverage in the Jura and unreliable velocity models. Indeed, discussions on the depth-distribution of earthquakes are somehow speculative. Publications of the SED indicate that the records of the seismic data could have several *quality ranks*, from A to D, depending on the distance of the events from the stations and the angular gap of the network. The majority of earthquakes used to compute the mechanisms have an A or B quality rank, which means that the vertical uncertainties are between 3 and 10 km. This value can exceed 10 km for the quality ranks C and D (e.g., Baer et al., 2005). In the following, we considered depths by steps of 5 km and discussed them in terms of in-basement rooted (for events deeper than 10 km) and not clearly in-basement rooted (events between 0

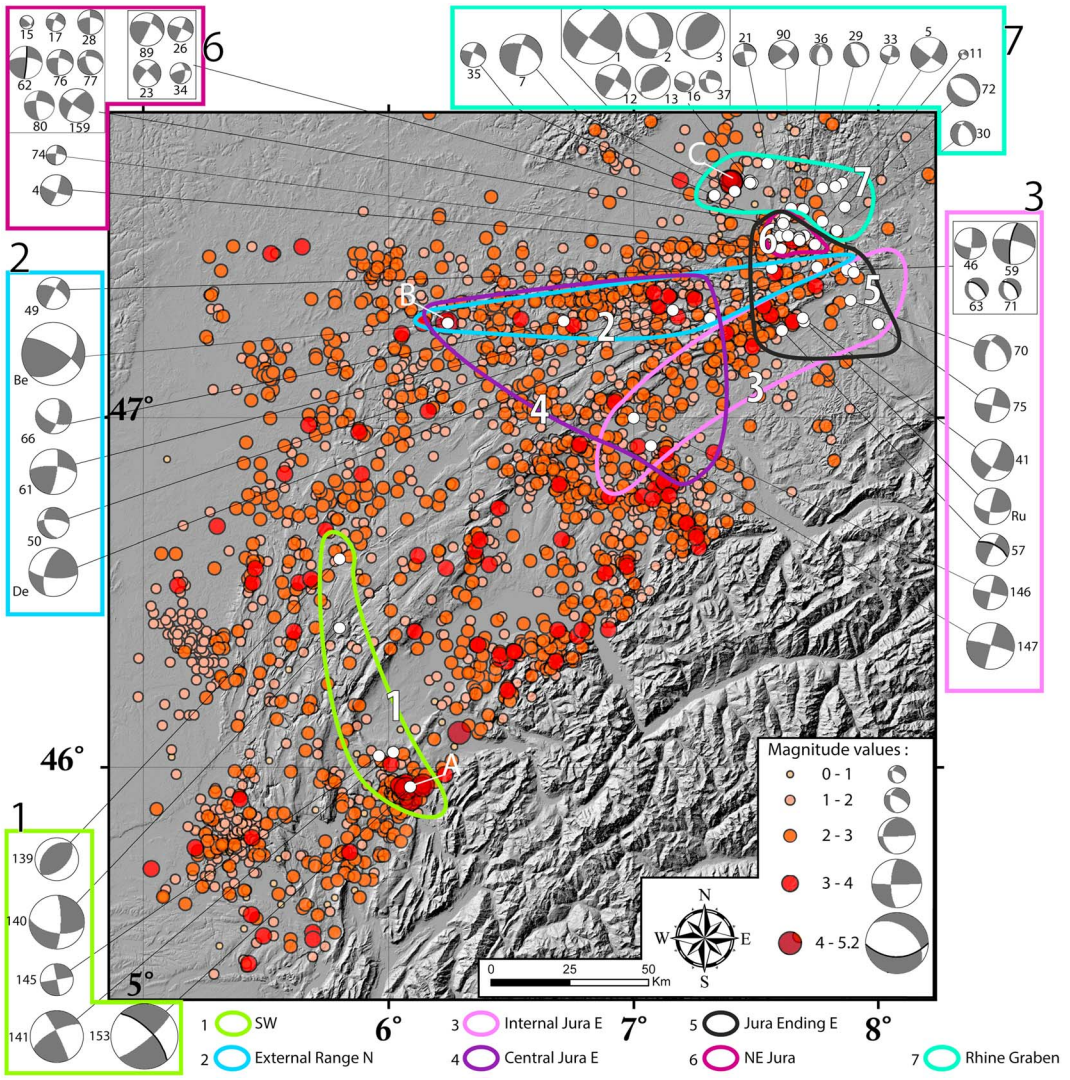

Figure 3. Seismicity of the Jura Mountain between 1971 and 2012 recorded by the French Alpine Seismic Network, the French National Seismic Monitoring Network, and the Swiss Seismological Service. The station locations of these three networks around the Jura Mountains are presented on Figure 4. The three white letters on the map correspond to the three biggest events: (a) 1996 Vuache earthquake (M_l 5.2); (b) 2004 Besançon earthquake (M_l 4.8); and (c) 1980 Sierentz earthquake (M_l 4.7). The 54 focal mechanisms computed in the Jura Mountains and its vicinity between 1971 and 2015 are compiled from Kastrup et al. (2004), Baer et al. (2005), and Deichmann et al. (2006, 2012). Seven so-called *inversion zones* have been determined based on the spatial distribution of mechanisms and structural pattern of the arc (numbered and colored shapes on the map, zones 4 and 5 include focal mechanisms of zones 2 and 3 and 2, 3, and 6, respectively).

and 5 km). The frequency-magnitude distribution (Figure 5a) follows the Gutenberg Richter law (Gutenberg & Richter, 1942, 1956) with a *b* value of 0.93 for magnitudes higher than the magnitude of completeness of about $M_c = 2$.

3.2. Focal Mechanisms

Focal mechanisms have been compiled from Kastrup et al. (2004) and the publication of the SED between 1999 and 2014 (Baer et al., 2005; Deichmann et al., 2006, 2012). These authors have completed the data from the SED network with those from the French National Seismic Monitoring Network and French Alpine Seismic Network (light colors on Figure 4) to better constrain the event locations and to improve the focal mechanisms.

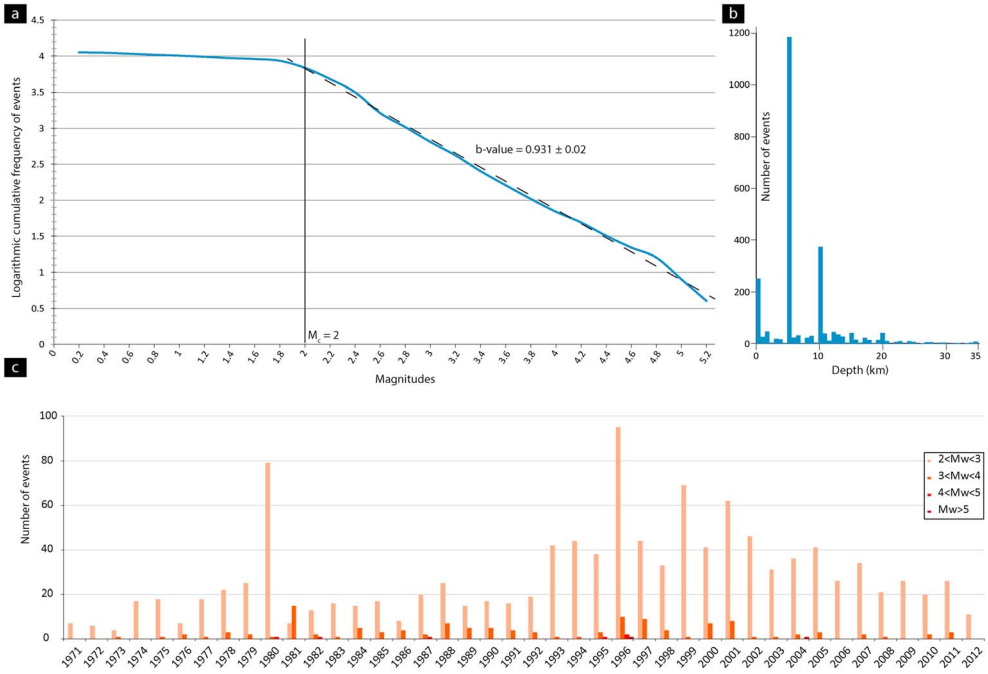

Figure 4. Seismic network around the Jura Mountains. The full colored stations are included in the Swiss Seismological Service (SED) network, which has been used to compute the majority of the focal mechanisms. Stations in shaded colors are those of French National Seismic Monitoring Network and French Alpine Seismic Network used to complete the SED data when necessary.

Among the 54 focal mechanisms compiled, 33 show strike-slip faulting, and 16 others show oblique slips associated with a normal (9) or an inverse (7) component (Figure 3). Only four mechanisms correspond to pure normal faulting. They are located at the northeastern end of the Jura Mountains. Four other focal mechanisms have a strong normal component in this area. These mechanisms could be related to the Rhine Graben activity (e.g., Becker, 2000). Three mechanisms of the 54 have a major reverse component, two of which are located at the southern edge of the Rhine Graben and the two others occurred in the folded Jura. The detailed parameters of the 54 focal mechanisms are listed in Table 1. Note that the configuration of the seismic networks around the Jura largely controls the spatial density of focal mechanisms (e.g., in the northeastern part of the Jura; Figure 4).

3.3. Stress Inversions

Based on their locations in the Jura Mountains, their internal deformation mode, and their location with respect to the Jura's structure, seven areas (called hereafter *inversion zones*) have been determined in order to compute homogeneous stress inversions (Figure 3). Zone 1 corresponds to the focal mechanisms located in the southern part of the Jura and in the vicinity of the Vuache fault (see above). The northeastern part has been separated into six inversion zones in order to test different configurations of inversion and discriminate potential variations in the overall stress pattern (Figure 3). Focal mechanisms along the External Range have been separated from those along the High Range or in the Molasse Basin in the vicinity of the High Range (zones 2 and 3, respectively, on Figure 3). A part of these two zones has been included in the Central Jura inversion (zone 4) to compare this stress field with the stress fields that could be under the influence of the Rhine Graben. The northeastern tip of the Jura Mountains has been analyzed in one zone (zone 5, called *Jura ending East*, in Figures 3 and 6) independently of the Rhine Graben zone (zone 7). A small inversion zone (zone 6) has been determined immediately south of the Rhine Graben in order to compare with the Rhine Graben zone (zone 7) and test its spatial influence.

Stress inversions have been performed using the software package MSATSI (Hardebeck & Michael, 2006; Lund & Townend, 2007; Martínez-Garzón et al., 2014) in a MATLAB environment. This software performs inversions using the linear method described in Michael (1984, 1987, 1991). Each inversion zone has been

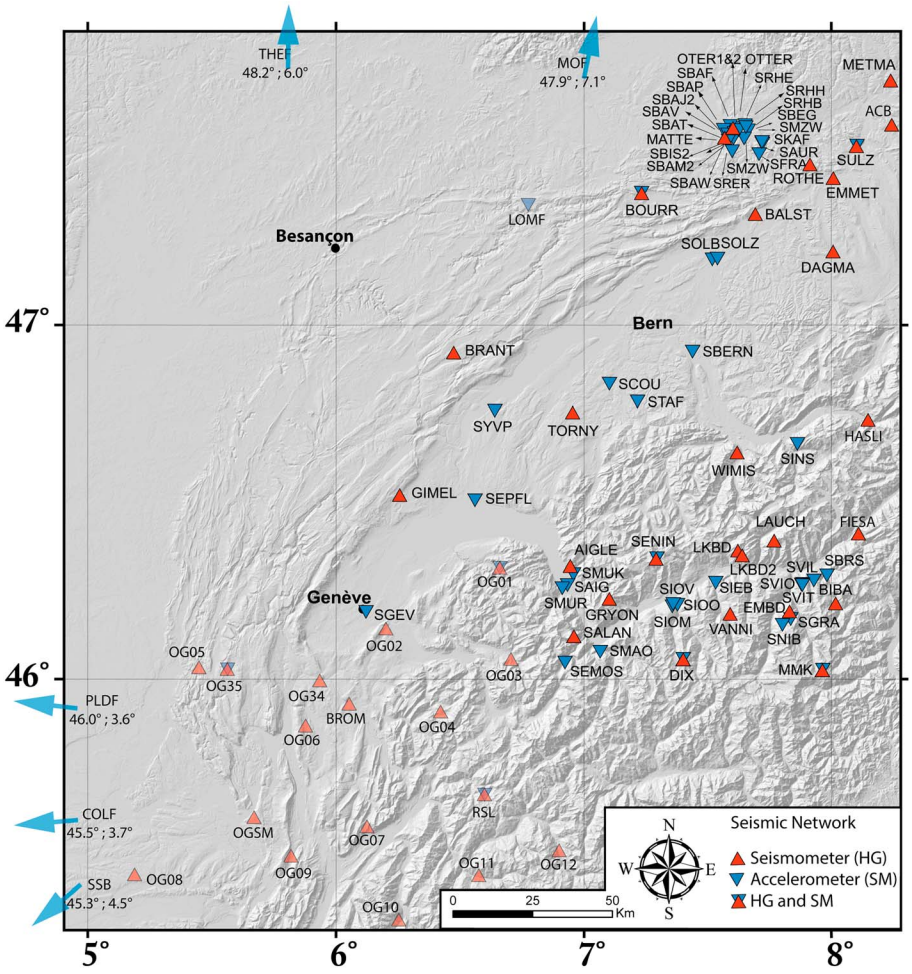

Figure 5. Statistical characterization of earthquakes within the Jura Mountains. (a) Frequency-magnitude distribution (blue curve) compared with the Guttenberg-Richter law (dashed black line), with a *b* value of 0.9. The magnitude of completeness (M_c = 2) corresponds to the magnitude for which the frequency of the recorded events leave the Guttenberg-Richter law, implying that the considered network does not record all the events below this magnitude. (b) Depth distribution of recorded events. Depending on the catalog, undetermined focal depth is fixed to 0, 5, or 10 km. Note that the overall depth determination is quite uncertain in particular due to the raw velocity model. (c) Magnitude-time distribution of events. Only the events having a $M_l > M_c$ are presented. See the main text for further information.

analyzed independently, and a last inversion has been realized using all focal mechanisms available in the Jura Mountains (Figure 6). Detailed results for each inversion are presented on Figure 7. In terms of methodology, the focal mechanism inversion relies on the same approach as fault slickenside analyses. They are based on the Wallace and Bott principle (Bott, 1959; Wallace, 1951), which has long been discussed and still remains a matter of debate concerning stress versus strain results (e.g., Angelier, 1990; Angelier & Goguel, 1979; Angelier & Mechler, 1977; Gephart, 1990; Lacombe, 2012; Twiss & Unruh, 1998; Yamaji, 2000, 2003; Yamaji & Sato, 2006, and references therein). Regardless of whether the stress or kinematic hypothesis is assumed, this principle states that fault slip parallels the direction of maximum resolved shear stress (on the considered plane) of the local spatially homogeneous stress tensor. Stress inversion methods assume a uniform state of stress within the study area as well as newly formed faults. Furthermore, in contrast to the inversion of fault-striae data, standard inversion of earthquake data (e.g., Delvaux, 1993; Gephart, 1990; Michael, 1987) does not a priori discriminate between the actual and the auxiliary nodal plane. Despite such restrictions, stress inversion has been shown to provide a powerful tool to analyze focal plane mechanism data sets (e.g., in the Alpine realm: Sue et al., 1999; Kastrup et al., 2004; Delacou et al. 2004). We refer to Champagnac et al. (2003), Delacou et al. (2004), and Lacombe (2012) for a complete discussion on these methods.

Table 1
Parameters of the 54 Focal Mechanisms Used in This Study

							First nodal plan			Second nodal plan			*P* axis		*T* axis		
FPS	Date	Time	Lat	Lon	*z*	ML	Strike	Dip	Rake	Strike	Dip	Rake	Strike	Dip	Strike	Dip	Location
1	15 July 1980	1217	47.67	7.48	12	4.7	125	80	174	216	84	10	350	3	81	11	Sierentz
2	15 July 1980	1254	47.67	7.49	10	3.7	117	46	−132	349	58	−55	314	60	55	6	Sierentz
3	16 July 1980	1500	47.67	7.48	13	3.8	201	42	64	54	53	111	129	6	21	72	Sierentz
4	25 March 1982	1845	47.49	7.6	7	2.5	110	79	−172	18	82	−11	334	13	64	2	Reinach
5	4 October 1982	406	47.67	7.85	23	2.9	36	74	−6	128	84	−164	353	15	261	7	Wiesental
7	28 February 1985	2133	47.65	7.41	10	3.4	292	49	−169	195	82	−41	145	34	250	21	Sierentz
11	1 November 1986	401	47.57	7.77	19	1.2	296	81	−174	205	84	−9	160	11	251	2	Dinkelberg
12	18 July 1987	859	47.67	7.48	12	2.8	299	80	177	30	87	10	164	5	255	9	Sierentz
13	21 November 1987	1401	47.68	7.48	12	2.8	209	38	64	61	56	109	138	9	18	72	Sierentz
15	31 December 1987	1516	47.52	7.68	12	1.1	53	40	14	312	81	129	13	26	258	41	Pratteln
16	23 March 1988	2111	47.68	7.47	11	1.6	7	30	−13	108	84	−119	350	44	222	33	Sierentz
17	11 May 1988	1112	47.52	7.68	10	1.5	199	75	−16	293	75	−164	156	22	66	0	Pratteln
21	20 November 1988	2043	47.73	7.55	17	1.9	263	68	−177	172	87	−22	125	17	220	13	Bad Bellingen
23	5 May 1989	1744	47.56	7.61	10	2.2	312	79	−170	220	80	−11	176	15	266	1	Basel
26	16 June 1990	2241	47.58	7.62	18	2	293	80	177	24	87	10	158	5	249	9	Weil
28	25 July 1990	1438	47.52	7.67	10	2	180	86	−32	272	58	−176	131	25	231	19	Pratteln
29	31 July 1990	1913	47.66	7.77	19	2	318	21	−109	158	70	−83	80	64	243	25	Steinen
30	28 November 1990	138	47.54	7.83	18	2	319	48	−130	190	55	−55	159	61	256	4	Mohlin
33	20 May 1991	13	47.66	7.82	17	1.5	105	73	−170	12	80	−17	328	19	59	5	Hausern
34	4 June 1991	1717	47.55	7.61	7	1.7	360	56	24	256	70	144	311	9	213	39	Basel
35	25 August 1991	6	47.64	7.33	12	2	292	76	−172	200	82	−14	155	16	247	4	Mulhouse
36	5 November 1991	913	47.6	7.69	17	1.8	334	43	−122	194	55	−64	160	68	266	7	Lorrach
37	12 November 1991	1910	47.68	7.48	12	1.8	175	59	−22	277	71	−147	139	36	44	8	Sierentz
41	13 August 1978	402	47.29	7.69	24	3.4	121	66	−168	26	79	−24	341	25	75	8	Onsingen
46	3 September 1982	1912	47.42	7.9	11	2.5	97	70	−175	5	85	−20	319	18	53	10	Hauenstein
49	10 April 1984	1650	47.43	7.57	22	2.6	300	62	−176	208	87	−28	160	22	257	17	Breitenbach
50	12 April 1984	50	47.44	7.75	21	2.5	162	42	−30	275	71	−128	143	49	32	17	Bubendorf
57	8 January 1987	1924	47.26	7.61	6	2.6	**298**	**62**	**−174**	205	85	−28	158	23	255	16	Gunsberg
59	11 April 1987	314	47.43	7.87	7	3.4	**190**	**76**	**−11**	282	79	−166	146	18	56	2	Laufelfingen
61	11 December 1987	225	47.31	7.16	79	3.7	274	70	168	8	79	20	140	6	232	22	Glovelier
62	16 December 1987	936	47.52	7.68	9	2.7	**6**	**86**	**36**	273	54	175	134	21	236	28	Pratteln
63	16 April 1988	1405	47.44	7.89	9	1.9	**310**	**63**	**−108**	165	32	−59	187	67	53	16	Zeglingen
66	30 April 1989	338	47.28	6.72	19	2.9	115	61	−156	13	69	−31	332	36	66	5	Belleherbe
70	15 December 1996	449	47.34	7.89	20	3	313	50	141	195	61	−47	158	53	256	6	Olten
71	21 February 1997	504	47.42	7.88	8	1.8	**316**	**55**	**−114**	174	42	−60	171	69	63	7	Laufelfingen
72	2 September 1997	30	47.61	7.86	23	2.6	128	53	−90	308	37	−90	38	82	218	8	Mohlin
74	27 October 1988	2052	47.5	7.74	12	1.6	275	77	−177	184	87	−13	139	11	230	7	Liestal
75	11 August 1990	531	47.27	8	15	2.8	11	90	0	281	90	180	326	0	236	0	Zofingen
76	16 August 1990	1839	47.52	7.6	11	2.1	282	61	−167	186	79	−30	140	29	237	12	Reinach
77	8 November 1990	1938	47.52	7.7	11	2	282	50	−141	164	61	−47	127	53	225	6	Pratteln
80	25 March 1992	533	47.52	7.63	8	2.6	278	65	−160	179	72	−26	137	31	230	5	Muttenz
89	24 April 1996	936	47.57	7.61	12	2.7	292	55	174	25	85	35	153	20	254	28	Basel
90	15 June 1996	105	47.6	7.64	21	2.4	314	73	165	48	76	17	180	2	271	23	Base
139	5 February 1968	228	46.6	5.8	6	3.5	224	38	90	44	52	90	134	7	314	83	Clairvaux
140	21 June 1971	725	46.4	5.8	3	4.4	99	57	−166	1	78	−34	315	32	54	14	Jeurre
141	29 May 1975	32	46.04	6.02	0	4.2	242	70	174	334	84	20	106	10	200	18	Vuache
145	16 November 1983	27	46.03	5.96	4	2.6	349	90	0	79	90	−180	304	0	34	0	Vuache
146	22 March 1976	1444	47	7	0	2.7	13	90	0	283	90	180	148	0	58	0	St.Blaise
147	3 July 1979	2113	46.93	7.07	30	3.8	285	86	179	15	89	4	150	2	240	4	Murten
153	15 July 1996	13	45.94	6.09	2	5.3	**316**	**70**	**−11**	50	80	−160	274	22	181	7	Annecy
159	13 July 1999	2047	47.51	7.7	19	2.7	215	70	−5	307	85	−160	173	17	79	11	Pratteln
Be	23 February 2004	1731	47.2	6.3	15	4.8	17	31	30	137	47	24	359	16	253	44	Besançon
De	27 December 2011	629	47.3	7.3	11	3.1	184	70	150	285	62	23	146	5	52	35	Délémont
Ru	12 May 2005	138	47.3	7.7	25	4.1	188	63	172	282	83	27	322	13	58	24	Rumisberg

Note. Data set compiled from Kastrup et al. (2004), Baer et al. (2005), and Deichmann et al. (2006, 2012). FPS = fault plane solution number; ML = local magnitude. In bold, prefered fault plane determined for 6 of the mechanisms.

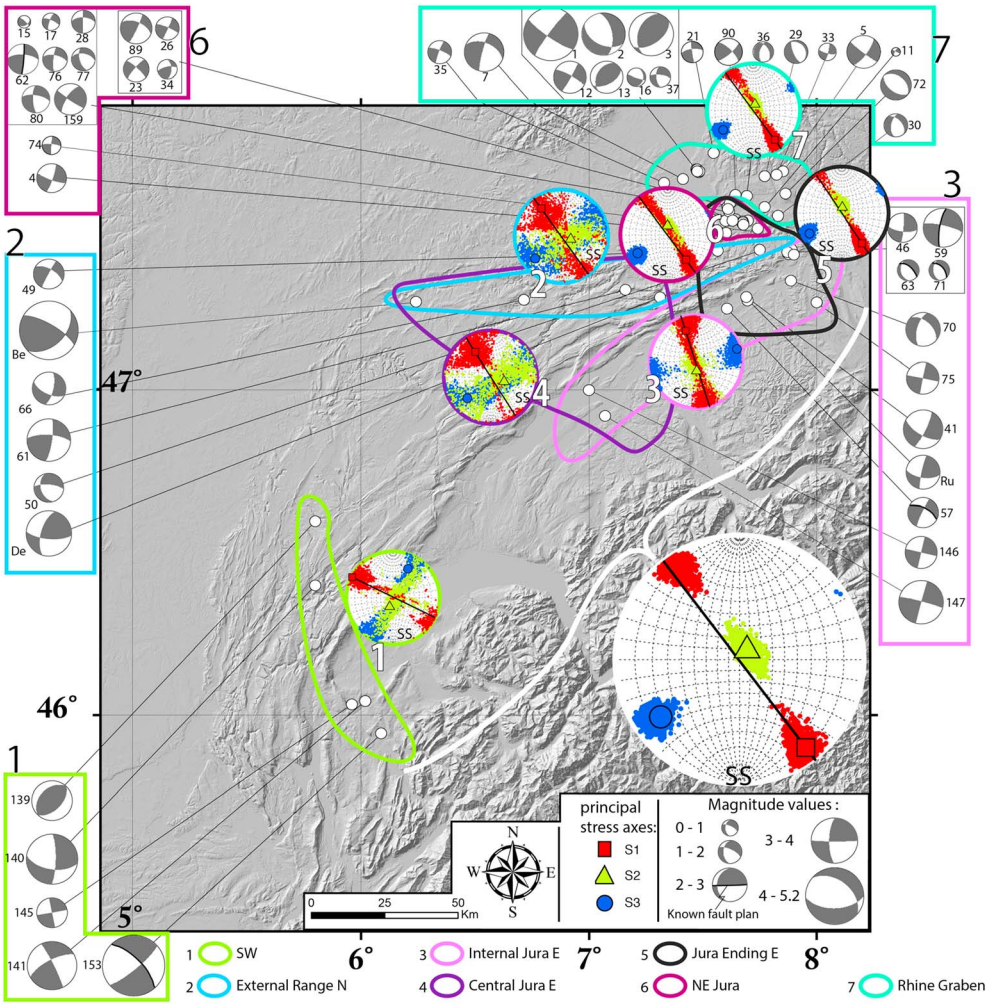

Figure 6. Results of the seismic inversions for each considered *inversion zone* (colored stereograms) and for the entire arc (white stereogram, right bottom angle). The three stress axes have been reported on the lower hemisphere of Wulff nets. The scattered points on each stereogram correspond to the 2,000 results of the bootstrapping method.

Whatever the inversion strategy (i.e., different zones tested), the stress tensor orientation is remarkably stable in the northern half of the Jura arc with a NNW-SSE oriented sigma1 (Figures 6 and 7). A rotation of 30° to 45° is observed in the southern zone with sigma1 oriented WNW-ESE. The inversion including all focal mechanisms, as well as those obtained from each inversion zone, is consistent with a strike-slip regime as defined by Zoback (1992) with a sigma1 direction of N143°E and sigma3 direction of N234°E (Figure 6).

In detail, due to the heterogeneity of the included focal mechanisms and the small amount of data, the inversions performed for the *External Range* (zone 2) and *Central Jura E* (zone 4) inversion zones show very scattered results. However, the best-fit stress tensors (actually the so-called deviatoric stress tensors) show similar sigma1 directions of N324°E and N328°E, respectively.

In the northeastern part of the Jura Mountains, three computed inversions (zone 7, zone 5, and zone 6 on Figure 6) show similar stress-axis directions. It is worth noticing that the stress tensor is homogeneous through the folded Jura and Rhine Graben limit.

In the southern part of the Rhine Graben (corresponding to the zones 5, 6, and 7), the depth distribution of the seismic events shows that the vast majority of earthquakes occurred between 15- and 30-km depth (Figure 8, black square). Moreover, many events have been located at more than 15-km depth in the northeastern most end of the folded Jura, which is in agreement with current deformation of the basement (e.g., Lacombe & Mouthereau, 2002). In order to test the heterogeneity of the stress field with depth, we have

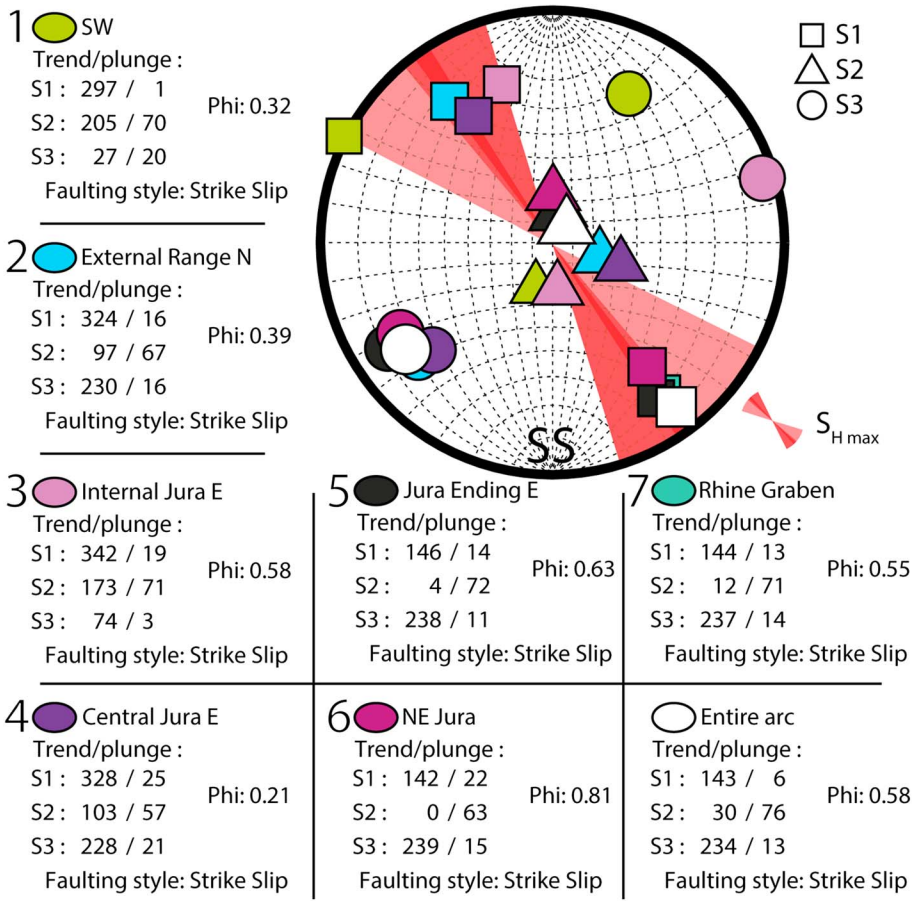

Figure 7. Best-fit stress tensors of the eight computed inversions reported on the lower hemisphere of a Wulff net. The shaded red zone on the stereogram represents the distribution of the determined sigma1 strikes. Phi reflects the relative stress magnitude (shape ratio) with $\varnothing = \frac{\sigma_2 - \sigma_3}{\sigma_1 - \sigma_3}$ (Martínez-Garzón et al., 2014).

computed four additional inversions including all the northeastern part of the Jura arc (i.e., inversion zones 5, 6, and 7) classified by depth locations of 5–10, 10–15, 15–20, and 20–30-km depth. Only one mechanism is available above 5-km depth, preventing inversion computation, but this mechanism shows a NE-SW sigma1 orientation with a strike-slip faulting style (FM no. 146; Figures 3, 6, and 8 and Table 1). These inversions show that the stress field remains remarkably steady with depth. This observation does not allow us to discuss the coupling or decoupling of the folded cover with the basement but shows a homogeneous stress tensor with depth in the northeastern part of the Jura. However, because of earthquake depth uncertainties, we cannot unambiguously discriminate earthquakes within cover sequences from upper crustal events.

In the western and southern parts of the Jura Mountains, the majority of earthquakes are located above 10-km depth (Figure 8).

4. GPS Data Analysis

4.1. Geodetic Surveys

The Jura Mountains are monitored by four networks of permanent GPS stations: AGNES (SwissTopo), Orpheon (Geodata Diffusion society), RGP (French permanent GPS network managed by IGN), and RENAG (French national GPS network for research purposes; RESIF, 2017; Figure 9). Since the end of the 1990s, permanent GPS stations have been installed all around the Jura arc, but the central Jura has been specifically instrumented only very recently. Between 2012 and 2014, five new stations have been installed (BLVR, FIED, FLGY, MRON, and PERX), and one old station has been reinstated (JOUX) in the central Jura in the

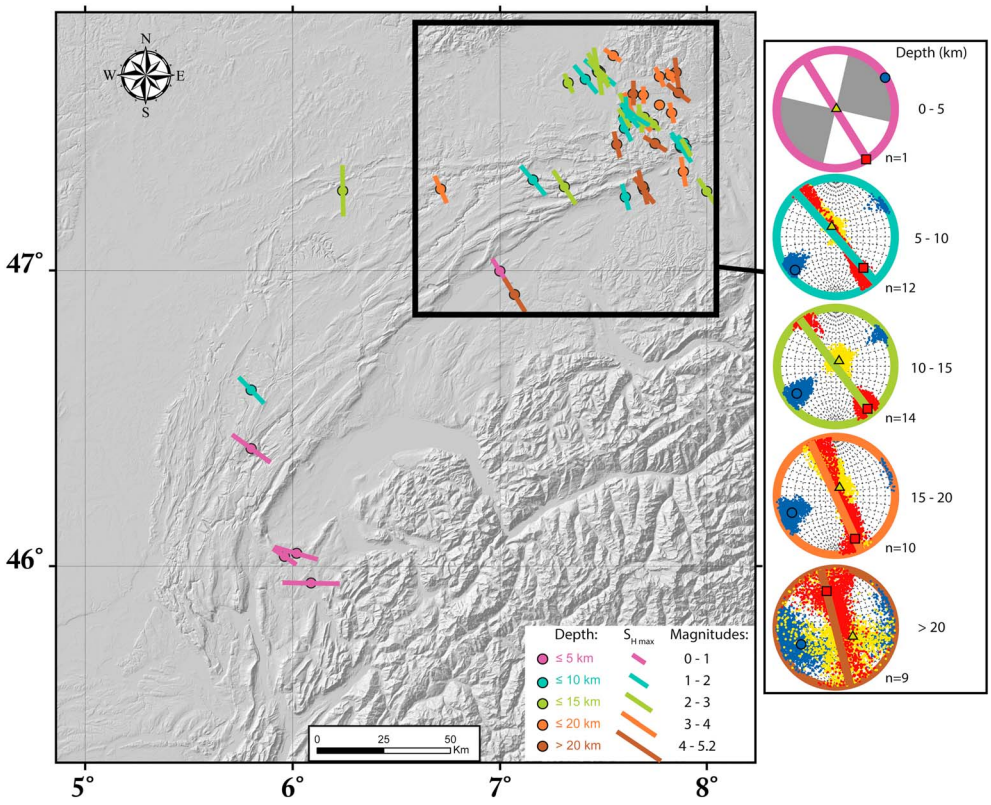

Figure 8. Depth distribution of recorded earthquakes in the Jura Mountains and its vicinity. The *P* axes orientations colored with respect to their depth location have been reported in the northeastern part of the arc. Four inversions have been computed in this eastern part with respect to the depth location of the events, and sigma1 orientations have been compared (lower hemisphere of Wulff net, right side).

framework of the GPS-JURA project (Besançon observatory OSU-THETA) and added to the RENAG network (Figure 9).

In this study, data from 63 permanent stations have been used, located over the European tectonic plate and including 35 stations within the Jura arc and its vicinity (Figure 9). The station coordinates and the observation span are presented together with the velocity results in Table 3.

The majority of these stations have been operational for more than 10 years (Figure 10). In the Jura Mountains' realm, 15 of the 35 stations have more than 8 years of recorded data. The last five stations from the GPS-JURA network have recorded less than 2 years of data, and we present here very preliminary results concerning these five specific stations (names with stars in Table 3).

4.2. Data Analysis

The analysis of the GPS data over the time span from January 2000 to March 2015 is done using the GAMIT/GLOBK version 10.5 software (Herring et al., 2010). Station coordinates and tropospheric parameters (one tropospheric zenith delay/2 hr and two couples of horizontal gradients/day) are estimated in daily sessions. IGS final orbits are held fixed. Tropospheric delay is estimated using the GMF tropospheric mapping function (Boehm et al., 2006) and a priori values of pressure and temperature at the GPS stations according to the GPT model (Boehm et al., 2007). Moreover, we implemented the ocean loading model FES2004 (Lyard et al., 2006) and the absolute antenna phase center variation model IGS08. Once the daily positions are established, we determine station velocities using the Kalman filter GLOBK. To obtain realistic velocity uncertainties, we apply the *real-sigma* strategy (Reilinger et al., 2006) that attributes an individual amount of colored noise to each station with respect to its observation span and the noise on its position time series. Typical values of colored noise estimated by the real-sigma strategy are 0.1/0.1/2.0 mm^2/year on the N/E/U

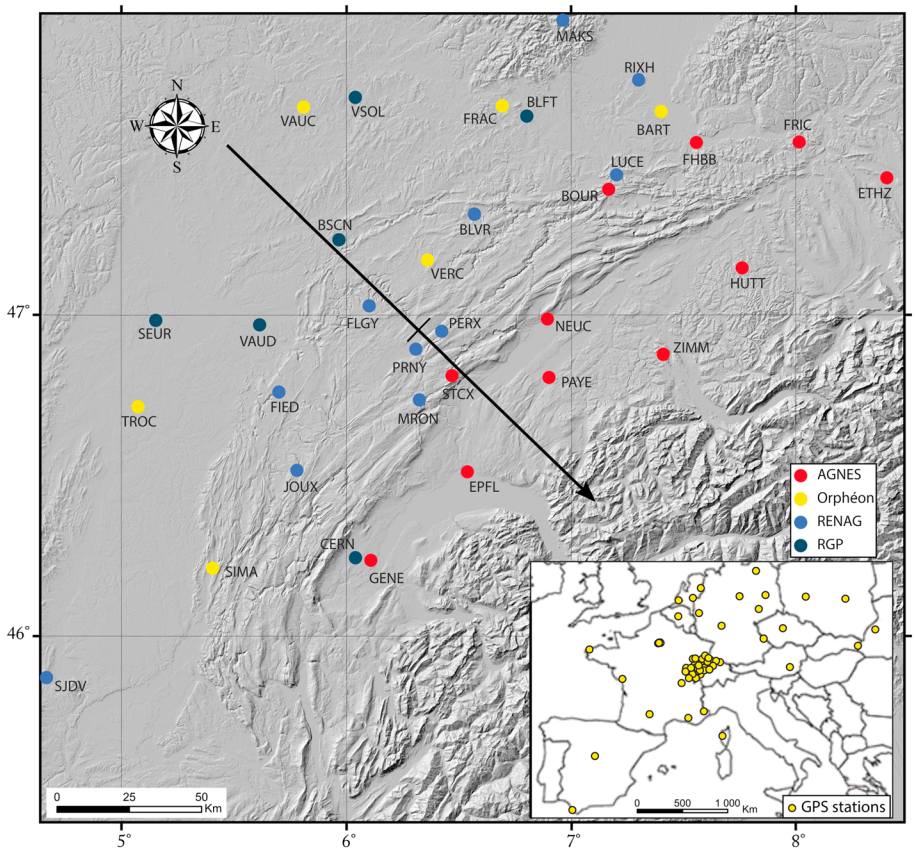

Figure 9. Network of permanent GPS stations in the Jura Mountains and its vicinity. The black line indicates the location of a range perpendicular profile for velocity profiles of Figure 12. The inset in the bottom right angle represents the locations of all the GPS stations included in our analysis.

coordinates. This amount of noise results in average velocity uncertainties of 0.19/0.18/0.58 mm/year (0.15/0.14/0.47 without the youngest station BLVR) on the N/E/U components, respectively. The reference frame has been established applying minimal constraints on 30 stations (AJAC, BOR1, BRST, BSCN, ETHZ, FFMJ, FRIC, GENE, GOPE, GRAS, GRAZ, JOZE, KOSG, LROC, LUCE, MAKS, MARS, NEUC, OPMT, POTS, SFER, SJDV, SULP, TLSE, VAUD, VILL, VSOL, WSRT, WTZR, and ZIMM) to project them onto their ITRF2008 velocities (Altamimi et al., 2012). Then, a solution with respect to stable Eurasia has been computed by minimizing the velocities of 27 Eurasian stations, yielding the Euler pole for the Eurasian plate (with respect to ITRF2008) indicated in Table 2.

This pole is consistent with the ITRF2008 solution including more Eurasian stations (Altamimi et al., 2012). Average amplitudes of both the north and east velocity residuals for the 19 stations constraining the Eurasian pole (position and angular velocity) are 0.20 mm/year, with individual values reaching −1.13 mm/year on the east component and 0.65 mm/year on the north component, respectively.

4.3. Geodetic Velocities and Deformation Rates

Horizontal and vertical velocities based on the analysis of the 63 permanent stations between 2000 and 2015 are presented in Table 3. Figure 11 shows horizontal velocities and their uncertainties in the Jura Mountains area with respect to stable Eurasia. Figure 12 represents arc perpendicular velocity profiles highlighting scatter in the horizontal, profile parallel (shortening/extension), and profile perpendicular (strike-slip) components, as well as in the vertical component. These profiles underline the relevance of data from stations older than 8 years. An average deformation tensor over the entire belt has been calculated using only this same group of stations older than 8 years and compared with calculations using all stations older than 5 years and using all the stations available (Figure 13). This strain rate tensor has also been plotted at the barycenter of these stations on Figure 14 and on the synthetic map of Figure 15.

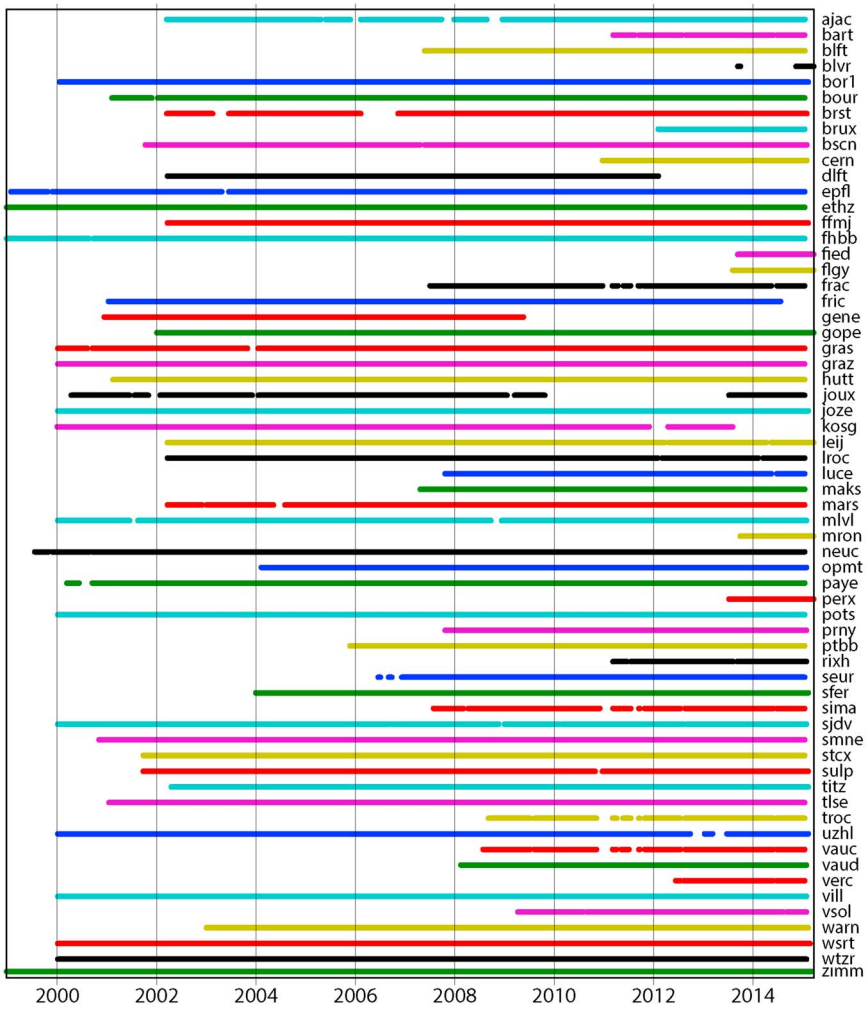

Figure 10. Period of GPS measurement for each station. The majority of the stations have more than 10 years of measurements.

The stations older than 8 years used to calculate the overall deformation axes are BOUR, BSCN, EPFL, ETHZ, FHBB, FRIC, GENE, HUTT, JOUX, NEUC, PAYE, SEUR, SJDV, STCX, and ZIMM. These stations are ideally distributed all around the Jura Mountains and show a low but significant NW-SE shortening of 2.86 ± 0.82 nanostrain/year (Figures 13, 14, and 15). It is coherent with the shortening rate of 1.88 ± 2.43 nanostrain/year obtained on the arc perpendicular profile, although this latter rate is not significant. Calculations using more recent stations show similar results, with a lower but still significant shortening axis also oriented approximately N345°E. Including the more recent stations in calculations increases the surface covered by stations that could explain the decrease of the amplitude of the calculated shortening rate.

Figure 11 and Table 3 indicate that most of the stations show velocities below 0.5 mm/year with uncertainties of about 0.1 mm/year. The only four stations showing displacement rates of 1 mm/year and more in the Jura

Table 2
Euler Pole Parameters Evaluated for the European Plate Motion With Respect to ITRF2008

Plate	W_x (deg/My)	W_y (deg/My)	W_z (deg/My)	RhoXY	RhoXZ	RhoYZ	Coord. system
Europe	−0.027117 ± 0.001083	−0.150083 ± 0.000205	0.207924 ± 0.001243	0.653	0.984	0.655	XYZ
Plate	Lat. (deg)	Lon (deg)	Mag (deg/My)	RhoLtLn	RhoLtMg	RhoLnMg	
Europe	53.740 ± 0.223	−100.242 ± 0.392	0.257862 ± 0.000818	0.978	0.971	0.974	LLM

Table 3
GPS Station Coordinates and Velocities (East, North, With Uncertainties and Correlation, Vertical With Uncertainties) With Respect to Stable Eurasia

Longitude (°)	Latitude (°)	V_e (mm/year)	V_n (mm/year)	σV_e (mm/year)	σV_n (mm/year)	Correlation (mm/year)	U (mm/year)	σU (mm/year)	Site name	First obs. used	Network
8.7626	41.9275	−0.09	0	0.13	0.12	0	−2.6	0.35	AJAC	2002.22	IGS/RGP
7.4796	**47.6331**	**−0.05**	**0.21**	**0.15**	**0.22**	**0.01**	**0.24**	**0.75**	**BART**	**2011.21**	**ORPHEON**
6.8585	**47.6259**	**0.24**	**−0.27**	**0.12**	**0.19**	**0**	**0.69**	**0.53**	**BLFT**	**2007.36**	**RGP**
6.6113	**47.3235**	**−0.19**	**1.36**	**2.7**	**2.75**	**0.02**	**11.59**	**6.75**	**BLVR***	**2014.86**	**RGP**
17.0735	52.277	−0.26	−0.31	0.06	0.07	0	1.09	0.29	BOR1	2000	IGS
7.2306	**47.3941**	**0.05**	**−0.08**	**0.07**	**0.07**	**0**	**0.23**	**0.32**	**BOUR**	**2001.1**	**AGNES**
−4.4966	48.3805	−0.18	0.61	0.17	0.14	0	3.1	0.38	BRST	2002.22	IGS/RGP
4.3586	50.7981	−0.94	−0.08	0.28	0.48	0	3.46	0.55	BRUX	2012.11	IGS
5.9894	**47.2469**	**0.25**	**−0.15**	**0.11**	**0.14**	**0**	**0.37**	**0.29**	**BSCN**	**2001.79**	**RGP**
6.0606	**46.257**	**−0.24**	**−0.28**	**0.15**	**0.15**	**0.01**	**−0.25**	**0.54**	**CERN**	**2011.02**	**RGP**
4.3876	51.986	0.08	−0.76	0.11	0.11	0	2.27	0.38	DLFT	2002.44	IGS
6.5679	**46.5215**	**0.04**	**0.48**	**0.11**	**0.18**	**0**	**0.74**	**0.4**	**EPFL**	**2000**	**AGNES**
8.5105	**47.4071**	**0.15**	**0.11**	**0.09**	**0.09**	**0**	**0.59**	**0.25**	**ETHZ**	**2000**	**AGNES**
8.665	50.0906	−0.38	−0.4	0.18	0.17	0	0.91	0.42	FFMJ	2002.44	IGS
7.6386	**47.5339**	**0.19**	**−0.01**	**0.1**	**0.1**	**0**	**0.43**	**0.34**	**FHBB**	**2000**	**AGNES**
5.7149	**46.7727**	**0.82**	**−1.09**	**0.46**	**0.48**	**0.03**	**3.22**	**2**	**FIED***	**2013.72**	**RENAG/RGP**
6.1262	**47.04**	**0.16**	**0.18**	**0.39**	**0.33**	**0.01**	**2.85**	**1.48**	**FLGY***	**2013.61**	**RENAG/RGP**
6.7456	**47.6597**	**−0.51**	**0.4**	**0.16**	**0.15**	**0**	**0.83**	**0.41**	**FRAC**	**2007.53**	**ORPHEON**
8.1119	**47.5274**	**0.15**	**−0.01**	**0.07**	**0.07**	**0**	**−0.09**	**0.31**	**FRIC**	**2001.01**	**AGNES**
6.1281	46.2483	0.05	0.39	0.14	0.16	0	−0.02	0.47	GENE	2000.95	
14.7856	49.9137	−0.19	−0.25	0.1	0.08	0	0.76	0.32	GOPE	2002	IGS
6.9206	43.7547	−0.03	−0.04	0.09	0.1	0	−1.2	0.26	GRAS	2000	IGS/RGP
15.4935	47.0671	0.98	0.37	0.18	0.09	0	−1.19	0.37	GRAZ	2000	IGS
7.8349	**47.1411**	**0.33**	**0.18**	**0.15**	**0.11**	**0**	**0.77**	**0.36**	**HUTT**	**2001.12**	**AGNES**
5.7957	**46.5286**	**0.25**	**0.1**	**0.09**	**0.09**	**0**	**0.42**	**0.32**	**JOUX**	**2000.3**	**RENAG/RGP**
21.0315	52.0973	−0.3	0	0.08	0.07	0	0.61	0.38	JOZE	2000	IGS
5.8097	52.1784	0.3	0.2	0.09	0.09	0	3.56	0.43	KOSG	2000	IGS
12.3741	51.354	0.07	−0.31	0.16	0.11	0	1.42	0.37	LEIJ	2002.44	IGS
−1.2193	46.1589	0	0.07	0.07	0.07	−0.01	0.95	0.25	LROC	2002.22	IGS/RENAG/RGP
7.2682	**47.4384**	**0.02**	**0.19**	**0.12**	**0.11**	**0**	**−0.2**	**0.41**	**LUCE**	**2007.83**	**RENAG/RGP**
7.0315	**47.923**	**0.16**	**−0.25**	**0.09**	**0.1**	**0**	**0.72**	**0.53**	**MAKS**	**2007.35**	**RENAG/RGP**
5.3538	43.2788	0.02	−0.26	0.12	0.13	0.01	−1.75	0.43	MARS	2002.22	IGS/RENAG/RGP
16.7045	40.6491	1	3.78	0.09	0.1	−0.01	−4.99	0.39	MATE	2000.01	IGS
2.5873	48.8411	0.29	−0.28	0.1	0.08	0	1.44	0.35	MLVL	2000.89	RGP
6.3524	**46.7472**	**1.2**	**−0.39**	**0.71**	**0.47**	**0.01**	**4.71**	**1.34**	**MRON***	**2013.75**	**RENAG/RGP**
6.9405	**46.9938**	**0.39**	**−0.25**	**0.07**	**0.08**	**0**	**−0.15**	**0.41**	**NEUC**	**2000**	**AGNES**
2.3349	48.8359	0.02	−0.34	0.08	0.07	0	1.92	0.34	OPMT	2004.11	IGS/RGP
6.9439	**46.8121**	**0.55**	**−0.49**	**0.08**	**0.08**	**0**	**−0.68**	**0.28**	**PAYE**	**2000.22**	**AGNES**
6.4562	**46.9601**	**2.6**	**−0.16**	**0.89**	**0.36**	**0.01**	**−3.48**	**1.07**	**PERX***	**2013.54**	**RENAG/RGP**
13.0661	52.3793	−0.3	−0.5	0.08	0.09	0	2.23	0.36	POTS	2000	IGS
6.3384	**46.9049**	**−0.55**	**−0.15**	**0.29**	**0.11**	**0**	**0.37**	**0.56**	**PRNY**	**2007.83**	**RGP**
10.4598	52.2962	−0.12	−0.18	0.09	0.1	0	2.35	0.4	PTBB	2005.89	IGS
7.378	**47.7333**	**−0.01**	**−0.16**	**0.14**	**0.17**	**0**	**0.04**	**0.6**	**RIXH**	**2011.19**	**RENAG/RGP**
5.1515	**46.9943**	**0.11**	**−0.25**	**0.1**	**0.1**	**0**	**0.33**	**0.36**	**SEUR**	**2006.93**	**RGP**
−6.2056	36.4644	−3.4	0.1	0.04	0.04	−0.01	−1.4	0.47	SFER	2004	IGS
5.4165	**46.2247**	**0.18**	**−0.33**	**0.16**	**0.35**	**0**	**−0.29**	**0.41**	**SIMA**	**2007.6**	**ORPHEON**
4.6766	**45.8791**	**0.07**	**−0.14**	**0.06**	**0.08**	**0**	**−0.16**	**0.28**	**SJDV**	**2000.01**	**RENAG/RGP**
2.425	48.8445	0.12	−0.21	0.11	0.1	0	2.33	0.33	SMNE	2000.88	RGP
6.5012	**46.8224**	**0.11**	**0.46**	**0.1**	**0.2**	**0**	**0.39**	**0.35**	**STCX**	**2001.72**	**AGNES**
24.0145	49.8356	−0.52	0.11	0.07	0.07	0	−0.54	0.38	SULP	2001.68	IGS
6.4316	51.0353	−0.02	−0.55	0.1	0.1	0	3.2	0.41	TITZ	2002.44	IGS
1.4809	43.5607	0.31	−0.16	0.08	0.1	0	−0.94	0.35	TLSE	2001.01	IGS/RGP
5.0751	**46.7256**	**0.26**	**−0.29**	**0.11**	**0.11**	**0**	**0.26**	**0.42**	**TROC**	**2008.71**	**ORPHEON**
22.2976	48.632	−0.41	−0.21	0.13	0.12	0	−1.4	0.52	UZHL	2000	IGS
5.8266	**47.6596**	**−0.14**	**−0.18**	**0.12**	**0.12**	**0**	**0.1**	**0.4**	**VAUC**	**2008.57**	**ORPHEON**
5.6269	**46.9812**	**0.35**	**−0.02**	**0.1**	**0.1**	**0**	**−0.29**	**0.38**	**VAUD**	**2008.14**	**RGP**
6.395	**47.1815**	**−0.33**	**0.03**	**0.38**	**0.22**	**0.01**	**−0.18**	**0.78**	**VERC**	**2012.5**	**ORPHEON**
−3.952	40.4436	−0.4	0.35	0.15	0.13	0	−1.88	0.43	VILL	2000	IGS

Table 3 *(continued)*

Longitude (°)	Latitude (°)	V_e (mm/year)	V_n (mm/year)	σV_e (mm/year)	σV_n (mm/year)	Correlation (mm/year)	U (mm/year)	σU (mm/year)	Site name	First obs. used	Network
6.0666	**47.6894**	**−0.08**	**−0.42**	**0.12**	**0.13**	**0**	**−0.12**	**0.42**	**VSOL**	**2009.28**	**RGP**
12.1014	54.1698	−0.5	−0.24	0.09	0.15	0	3.53	0.36	WARN	2003.12	IGS
6.6045	52.9146	−0.21	0.27	0.06	0.06	0	2.61	0.34	WSRT	2000	IGS
12.8789	49.1442	0.17	0.02	0.07	0.09	0	−0.04	0.38	WTZR	2000	IGS
7.4653	46.8771	0.05	0.22	0.06	0.06	0	0.86	0.27	ZIMM	2000	AGNES/IGS

Note. The observation span and the network of origin are indicated in columns 11 and 12. Bold lines correspond to stations within the Jura area. Site names with a star highlight the new central Jura stations of OSU THETA.

area have less than 2 years of measurements and correspond to the OSU THETA network (BLVR, FIED, MRON, and PERX). They should converge toward lower velocities in the future.

Considering only the stations older than 5 years, two provinces of homogeneous displacement can be identified (I and II on Figure 14). The first one corresponds to the northwestern and western foreland of the folded Jura, including, locally, a part of the external Range. In this province, seven stations show a consistent displacement of 0.29 ± 0.15 mm/year toward the southeast (BLFT, BSCN, SEUR, VAUD, TROC, SIMA, and SJDV). This province covers a part of the Bresse Graben and the RBTZ. The BSCN station is located in a particular zone

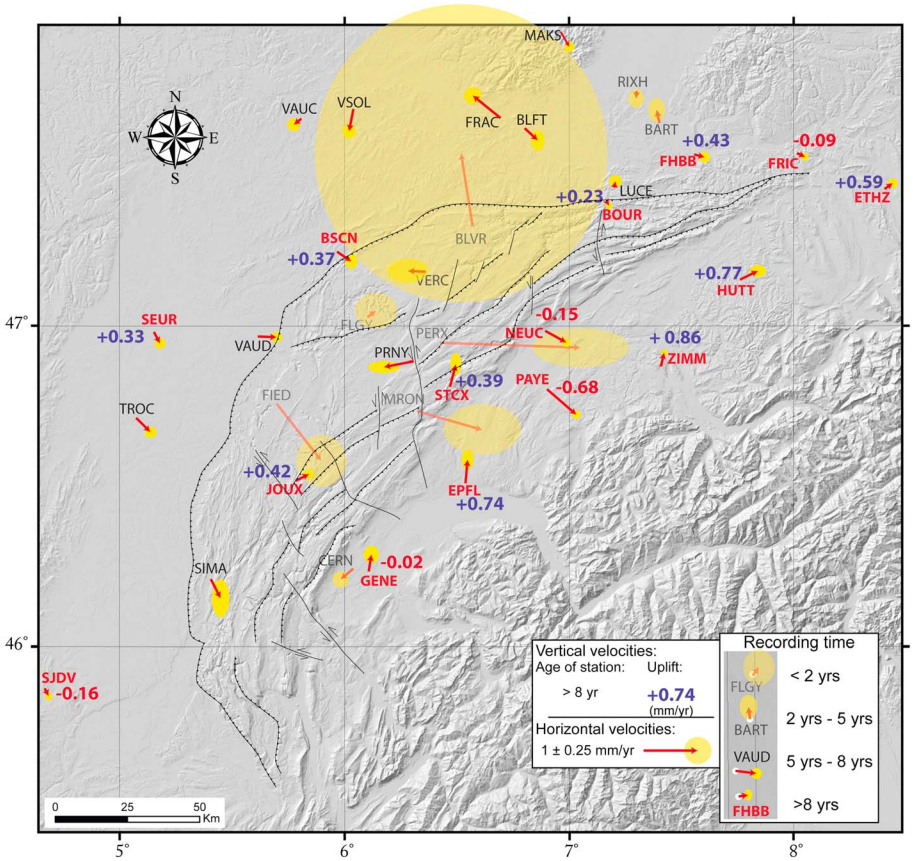

Figure 11. Map of geodetic horizontal velocities in the Jura Mountains and its vicinity. Most recent stations of the OSU THETA network (names with stars in Table 3) have very high uncertainties and have not been considered in the discussions (see Figure 13 for the most pertinent data). Vertical movements have also been reported for the stations older than 8 years.

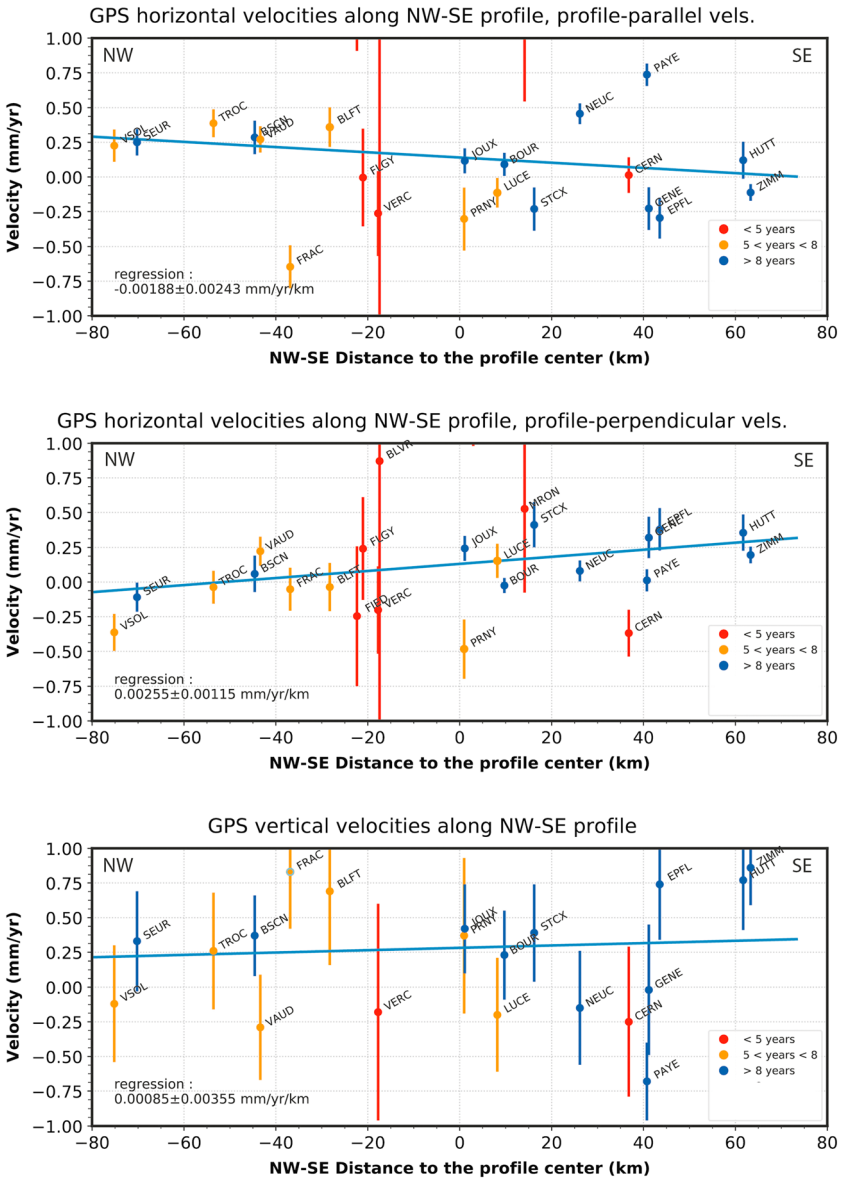

Figure 12. Arc perpendicular profiles of horizontal and vertical velocity components of GPS stations in up to 100-km distance from the profile (see location in Figure 9). Stations are plotted with respect to their distance along the profile. Color code indicates station age. The regressions are calculated only over stations older than 8 years. The upper graph represents the horizontal, profile parallel components (the negative slope corresponding to shortening along the profile). The middle graph shows the horizontal, profile perpendicular components (the positive slope corresponding to a general left-lateral displacement). The lower box highlights the vertical displacements along the profile, with an increase of upward motion toward the SE.

called the Besançon Zone, defined as the northwestern most segment of the thin-skinned Jura fold-and-thrust belt (Madritsch et al., 2008). This zone is also affected by crustal-scale Paleogene normal faults of the RBTZ system (Bergerat & Chorowicz, 1981; Illies & Greiner, 1978; Madritsch et al., 2008, 2009). Madritsch et al. (2008) have shown that thick-skin deformation occurred in this particular area with the inversion of some of these faults and suggest a transpressional reactivation of the RBTZ structures. All these observations lead us to consider this zone as a particular structural area that could be disconnected from the rest of the folded Jura arc.

The SIMA station, included in the Province I, is located in the western part of the external Range, which suggests that the deformation of the surface in this part of the external Range could be linked to the deformation

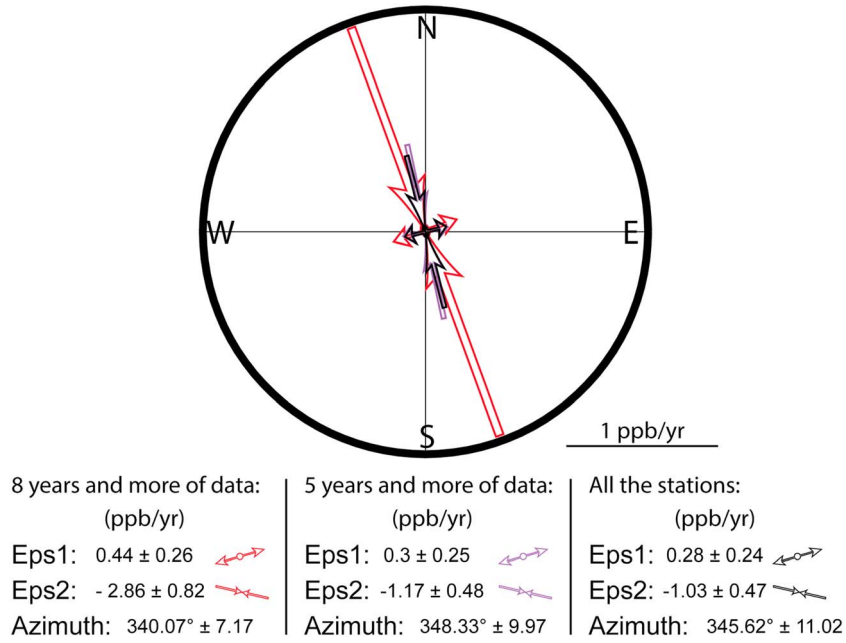

Figure 13. Deformation axes plotted in a directional diagram for strain calculation including stations older than 8 years (red empty arrows), older than 5 years (blue empty arrows), and for all the stations (black empty arrows).

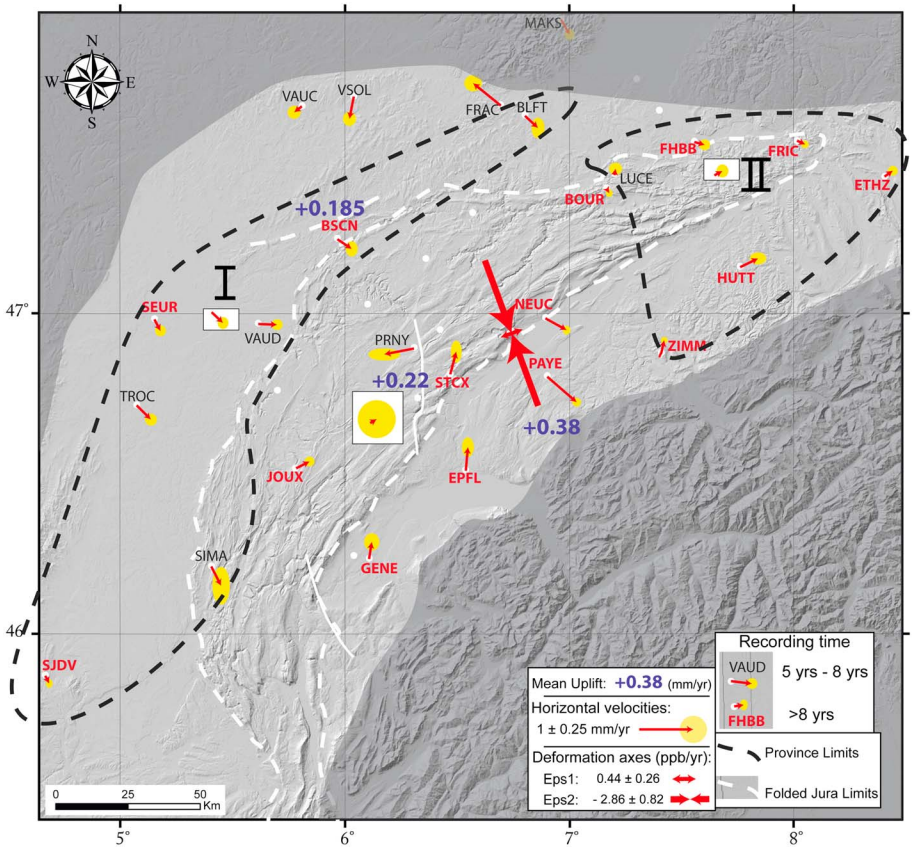

Figure 14. Map of horizontal geodetic velocities from stations older than 5 years in the Jura Mountains and its vicinity. Consistency between the directions of horizontal movements allows to define two provinces of homogeneous deformation (I and II). The mean displacement vector has been reported in a white square for the two provinces and for the central part of the Jura with its associated standard deviation (yellow ellipsoid).

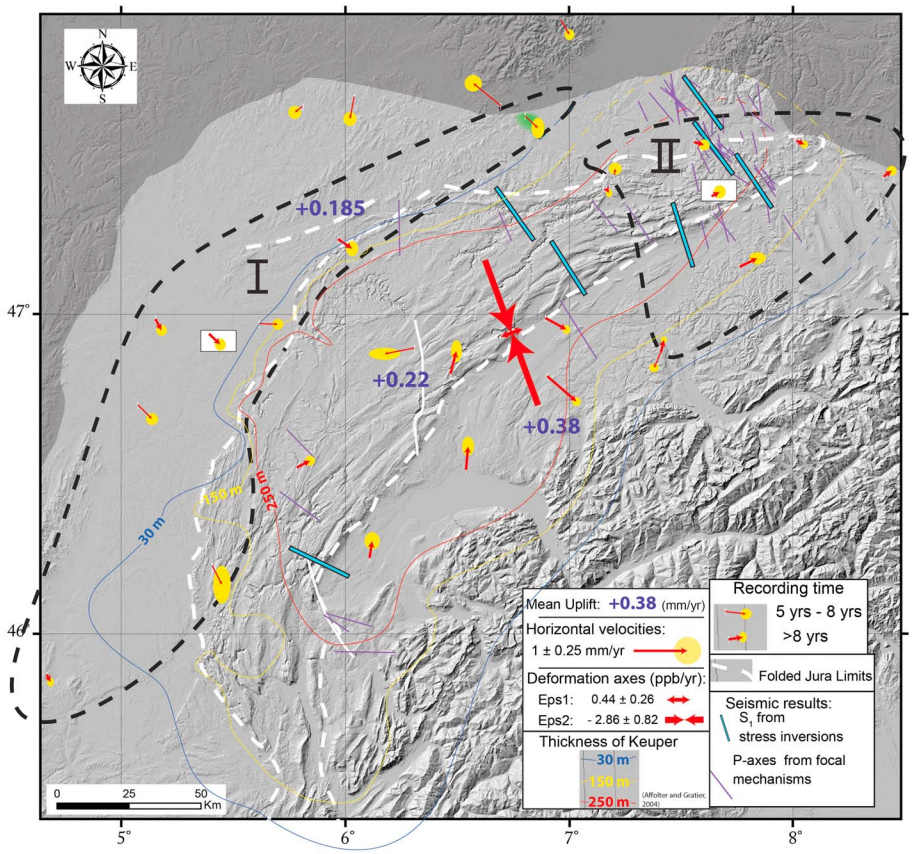

Figure 15. Synthetic map of geodetic velocities and seismic sigma1 orientations. Colored patches correspond to the extended area of GPS and seismic data included in the provinces I (green) and II (blue). In the northeastern part, the province II shows uniform deformation and stresses beyond the folded Jura limits. The lack of data does not allow to correctly characterize the neotectonic activity in the central part of the Jura Mountains. The distribution of the thickness of the Keuper reported from Affolter and Gratier (2004) allows to explain the limits between the different provinces.

of the Bresse Graben, further west. Becker (2000) has shown a similar repartition of the deformation based on in situ stress data that he explains by an influence of the Bresse Graben deformation on this part of the external Range.

A second province (II on Figure 14) could be identified in the eastern part comprising six stations showing consistent east to northeastward movements with 0.17 ± 0.16 mm/year (ETHZ, FHBB, FRIC, HUTT, LUCE, and ZIMM). HUTT is the only station showing a higher rate of 0.37 ± 0.15 mm/year. Its proximity with the Alps could explain this difference, but ZIMM does not show the same information. This province shows a homogeneous deformation field through the easternmost part of the Molasse basin, the eastern part of the folded Jura, and even beyond the northern frontal thrust of the Jura (FHBB). These data suggest that the GPS-measured deformation field around the eastern tip of the Jura Mountains is not constrained by the surface boundary of the belt.

Stations located in the central part of the folded Jura (JOUX, GENE, PRNY, STCX, EPFL, NEUC, and PAYE) show inconsistent movements with a nonsignificant average velocity. This finding suggests that measurement uncertainties are hiding the weak tectonic signal in this area.

The general strain rate tensor calculated from GPS velocities (Figure 13) has been reported on Figure 14. This tensor shows a low horizontal NW-SE shortening, but the lack of data in the central part does not allow calculating a significant strain rate tensor localized only in this central part of the Jura.

Concerning the vertical motions and considering the uncertainties of these values, only the data from the stations having 8 years or more of recording have been considered (Figures 11 and 12, lower graph). An average tendency of vertical motion has been calculated from the individual velocities (Figure 12). This average slope

shows an increase of uplift from the External Range toward the Alps. It comprises the maximum uplift of 0.86 ± 0.27 mm/year of the ZIMM station close to the Alps and two stations showing an uplift reduced to about 0.4 mm/year in the High Range and in the Central arc (STCX and JOUX), suggesting already a decrease of the uplift rate at the vicinity of the folded Jura. The uplift rate decreases even more to 0.3 mm/year just north of the External Range (BOUR, BSCN, and SEUR). The three stations located in the northeastern part of the Molasse Basin (ZIMM, HUTT, and ETHZ) indicate a similar tendency of diminution to the northeast, which seems controlled by the distance to the Alps. Our observations are coherent with a general uplift pattern constraint by geodesy in the western Alps, as shown recently for example, by Nocquet et al. (2016). Moreover, similar results about the uplift repartition have been obtained in the folded Jura in a previous study from geomorphologic data highlighting greater vertical movements in the High Range than in the External Range (Rabin et al., 2015).

5. Discussion and Concluding Remarks

The reassessment of the seismotectonic data combined with GPS observations over more than 15 years in the Jura arc and its vicinity allows us to discuss the actual 3D distribution of the current deformation and related stress over the belt. Seismic and geodetic data show consistent results, with a general NW-SE orientation for both compression and shortening axes arising from seismology and geodesy, respectively. Seismotectonic stress inversion showed that the overall stress field is transcurrent with a horizontal sigma3 axis oriented NE-SW and coherent with the small extensional strain axis determined from our GPS analysis (Figures 6, 7, 13, and 14). These data are consistent with the results of previous studies on the Rhine Graben and the Alpine Foreland (Kastrup et al., 2004; Plenefisch & Bonjer, 1997). Horizontal velocities, strain rate tensors from GPS stations, and horizontal sigma1 from seismic data have been reported on Figure 15 and regrouped by colored patches.

Using the seismological data, the easternmost province (II), determined from horizontal geodetic velocities, must be extended westward and northward to take into account all the consistent sigma1 orientations (Figures 14 and 15). Both geodetic and seismic data show that the strain rate and the stress fields (resp.) do not seem to be affected by the limits of the folded Jura. Similar observations have been proposed from in situ stress measurements (borehole) in this area (Becker, 2000). Displacements given by geodetic data are consistent with a general northeastward movement of the surface while the seismic data show a stress field characterized by a NW-SE sigma1. The depth distribution of earthquakes in this zone shows that the basement under the Jura cover is impacted by the current transcurrent deformation. According to these observations, the uppermost cover, characterized by an eastward displacement, would be decoupled from its basement. The thickness of the evaporite assuming the role of décollement level under the folded cover could explain the distribution of the deformation in the vicinity of the folded Jura (Figure 14 and Affolter and Gratier, 2004). Moreover, in situ stress measurements at the subsurface (30 m) have shown a N-S $S_{H\ max}$ orientation in this northeastern area suggesting an anticlockwise rotation of $S_{H\ max}$ between the surface and deep structures (Becker, 2000; Ustaszewski & Schmid, 2007). This rotation has been interpreted as an evidence of a mechanical decoupling of the cover from its basement (Ustaszewski & Schmid, 2007, and references therein). However, focal mechanisms and seismic inversions highlight a general strike-slip deformation mode throughout this area, which is not in agreement with a thrusting thick-skin deformation as defined in Coward (1983). These data suggest that the eastern part of the Jura Mountains is still in a NW-SE compressional field affecting the cover and the basement under a general strike-slip deformation mode.

The northern part of the province I corresponds to the RBTZ as defined by Madritsch et al. (2008, 2009). These authors suggest that at least a part of the RBTZ (Besançon Zone) is expected to be in transpressional regime within the cover and the coupled basement. The only focal mechanism available in this area is in line with this interpretation (noted Be in Table 1 and on Figure 6). This earthquake occurred in the basement of the folded Jura arc (Baer et al., 2005; Madritsch et al., 2008) and showed an oblique-slip deformation mode. Our geodetic data show significant and homogeneous displacement toward the southeast (with respect to the stable Europe) through the entire RBTZ and the northern part of the Bresse Graben, suggesting the same deformation field through this zone. Moreover, surface measurements (Becker, 2000), paleostress data (Ustaszewski & Schmid, 2006), and geodetic and seismological data are consistent with a transpressional regime, which

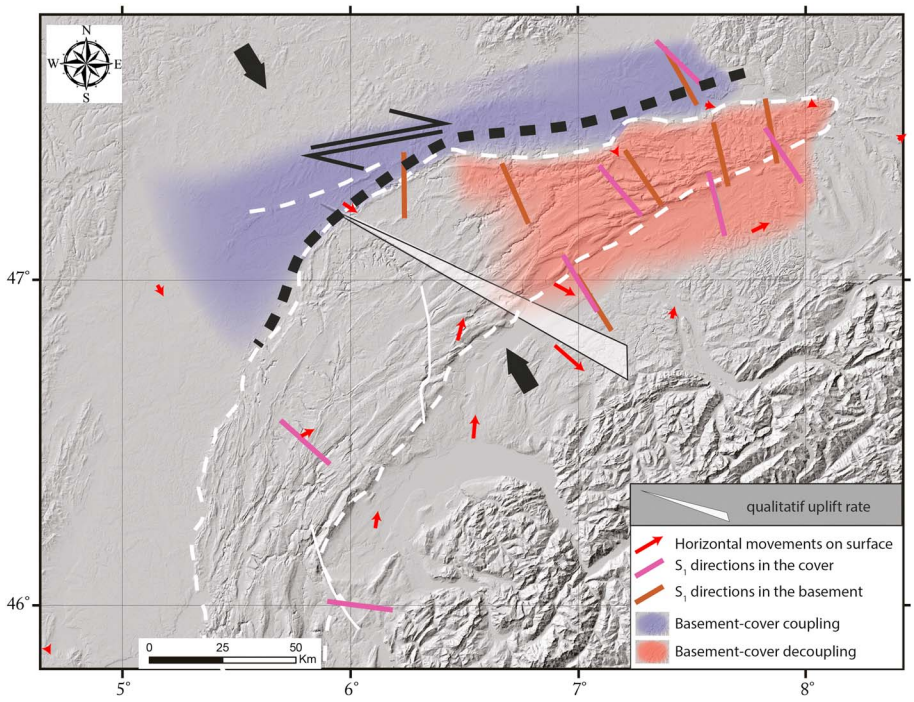

Figure 16. Interpretative map of the current deformation of the Jura and its vicinity. In the eastern part of the Jura, the cover seems to be decoupled from the basement while they seem coupled at the front of the Jura, in the Rhine-Bresse Transfer Zone. The extent of these two deformation modes in the central part of the Jura and in its western part is not enough constraint by available data and has not been represented here. The entire Alpine Foreland represented by the folded Jura, the Molasse Basin, and the front of the Jura is affected by a general uplift increasing toward the Alpine front where it reaches ~0.4 mm/year, which is in linear continuity with the uplift observed in the Alps (e.g., Nocquet et al., 2016, see text for details).

could affect the entire RBTZ, the southern part of the Rhine Graben, and eventually the eastern ending of the folded Jura (Figures 14 and 15). This deformation is expected to affect both the sedimentary cover and the coupled basement (Giamboni, Ustaszewski, et al., 2004; Madritsch et al., 2008, 2009; Ustaszewski & Schmid, 2007).

The southernmost part of the province I corresponds to the northern part of the Bresse Graben and the westernmost part of the External Range. In this area, there are only two GPS stations and no seismic data available. This part of the External Range has been connected with the Bresse Graben in terms of deformation according to in situ stress data in Becker (2000). Moreover, the distribution of the thickness of the Keuper under this area could explain the occurrence of two different deformation styles. One style would be affecting the RBTZ, the Bresse Graben, and the westernmost part of the external Range, corresponding to province I, where the basement and the cover could be coupled. Another style affects the central part of the folded Jura and the Molasse Basin where the cover could be decoupled from the basement and that could eventually be regrouped with the deformation mode observed in the northeastern part of the Jura (province II in Figure 15). A recent study based on microseismicity has highlighted evidence of decoupling between cover and basement in the central part of the Molasse Basin (Vouillamoz, 2015). These observations could support the existence of a deformation mode affecting the Molasse Basin that could differ from the deformation observed at the front of the Jura, the RBTZ, and the Bresse Graben.

Figure 16 summarizes the two tectonic provinces, coupled or not to their basement, according to our interpretation of the GPS velocity field in the Jura and its vicinity. Due to a lack of relevant data, the interpretation of this deformation cannot be extended to the central and the western parts of the Jura. GPS stations recently implemented in the central part of the folded Jura (GPS-JURA, part of the French RENAG network) together with new seismic stations (JURAQUAKE project and RESIF) will bring precious information in the near future to better constrain the distribution of the Jura's overall deformation.

Acknowledgments
This work has been carried out thanks to the financial support of OSU-THETA (Besançon observatory), Besançon and Grenoble Universities, and the Franche-Comte region (GPS-JURA) project. We thank the technical team of the OSU THETA for GPS-JURA network handling. The GPS data used in this study are publicly available data from the RESIF-RENAG network (http://renag.resif.fr), from the RGP network managed by IGN (Institut National de l'Information Géographique et Forestière, http://rgp.ign.fr) also contributing to RESIF, from the ORPHEON network of the society GEODATA DIFFUSION (http://orpheon-network.fr), and from the AGNES network of Swisstopo (http://pnac.swisstopo.admin.ch/pages/en/agnes.html). RESIF is a national Research Infrastructure, recognized as such by the French Ministry of higher education and research. RESIF is managed by the RESIF Consortium, composed of 18 Research institutions and universities in France. RESIF is supported by a public grant provided by the French National Research Agency (ANR) as part of the "Investissements d'Avenir" program (reference: ANR-11-EQPX-0040) and the French Ministry of Environment, Energy and Sea. ORPHEON GNSS data were provided to the authors for a scientific use in the framework of the GEODATA-INSU-CNRS agreement. AGNES GPS data were provided to the authors for a scientific use in the framework of an agreement between Besançon University and Swisstopo. We owe much to the Editor, Associated Editor, and three reviewers for their careful and constructive comments, which allowed us to greatly improve the manuscript. We thank B. Delacou, S. Schmid, and E. Kissling for fruitful discussions. We thank A. Fleuriot for editing advices.

References

Affolter, T., & Gratier, J. P. (2004). Map view retrodeformation of an arcuate fold-and-thrust belt: The Jura case. *Journal of Geophysical Research*, *109*, B03404. https://doi.org/10.1029/2002JB002270

Altamimi, Z., Métivier, L., & Collilieux, X. (2012). ITRF2008 plate motion model. *Journal of Geophysical Research*, *117*, B07402. https://doi.org/10.1029/2011JB008930

Angelier, J. (1990). Inversion of field data in fault tectonics to obtain the regional stress—III. A new rapid direct inversion method by analytical means. *Geophysical Journal International*, *103*(2), 363–376. https://doi.org/10.1111/j.1365-246X.1990.tb01777.x

Angelier, J., & Goguel, J. (1979). Sur une méthode simple de détermination des axes principaux des contraintes pour une population de failles. *Comptes Rendus. Académie des Sciences*, *288*, 307–310.

Angelier, J., & Mechler, P. (1977). Sur une methode graphique de recherche des contraintes principales egalement utilisables en tectonique et en seismologie: la methode des diedres droits. *Bulletin de la Société Géologique de France*, *S7–XIX*, 1309–1318. https://doi.org/10.2113/gssgfbull.S7-XIX.6.1309

Aubert, D. (1949). Le Jura. *Geologische Rundschau*, *37*(1), 2–17. https://doi.org/10.1007/BF01792491

Baer, M., Deichmann, N., Braunmiller, J., Husen, S., Fah, D., Giardini, D., et al. (2005). Earthquakes in Switzerland and surrounding regions during 2004. *Eclogae Geologicae Helvetiae*, *98*(3), 407–418. https://doi.org/10.1007/s00015-005-1168-3

Baran, R., Friedrich, A. M., & Schlunegger, F. (2014). The late Miocene to Holocene erosion pattern of the Alpine Foreland basin reflects Eurasian slab unloading beneath the western Alps rather than global climate change. *Lithosphere*, *6*(2), 124–131. https://doi.org/10.1130/L307.1

Becker, A. (2000). The Jura Mountains—An active foreland fold-and-thrust belt? *Tectonophysics*, *321*(4), 381–406. https://doi.org/10.1016/S0040-1951(00)00089-5

Bergerat, F., & Chorowicz, J. (1981). Etude des images Landsat de la zone transformante Rhin-Saône (France). *Geologische Rundschau*, *70*(1), 354–367. https://doi.org/10.1007/BF01764334

Boehm, J., Werl, B., & Schuh, H. (2006). Troposphere mapping functions for GPS and very long baseline interferometry from European Centre for Medium-Range Weather Forecasts operational analysis data. *Journal of Geophysical Research*, *111*, B02406. https://doi.org/10.1029/2005JB003629

Boehm, J., Cerveira, P. J. M., Schuh, H., & Tregoning, P. (2007). The impact of mapping functions for the neutral atmosphere based on numerical weather models in GPS data analysis. In D. P. Tregoning & D. C. Rizos (Eds.), *Dynamic planet*, *International Association of Geodesy Symposia* (pp. 837–843). Berlin Heidelberg: Springer. https://doi.org/10.1007/978-3-540-49350-1_118

Bott, M. H. P. (1959). The mechanics of oblique slip faulting. *Geological Magazine*, *96*(02), 109–117. https://doi.org/10.1017/S0016756800059987

Burkhard, M. (1990). Aspects of the large-scale Miocene deformation in the most external part of the Swiss Alps (subalpine Molasse to Jura fold belt). *Eclogae Geologicae Helvetiae*, *83*, 559–583.

Burkhard, M., & Sommaruga, A. (1998). Evolution of the western Swiss Molasse basin: Structural relations with the Alps and the Jura belt, in: Cenozoic Foreland basins of western Europe (Mascle et Al), *Geological Society of London, Special Publication*, *134*(1), 279–298. https://doi.org/10.1144/GSL.SP.1998.134.01.13

Carretier, S., Nivière, B., Giamboni, M., & Winter, T. (2006). Do river profiles record along-stream variations of low uplift rate? *Journal of Geophysical Research*, *111*, F02024. https://doi.org/10.1029/2005JF000419

Champagnac, J. D., Sue, C., Delacou, B., & Burkhard, M. (2003). Brittle orogen-parallel extension in the internal zones of the Swiss Alps (south Valais). *Eclogae Geologicae Helvetiae*, *96*, 1–14.

Champagnac, J. D., Molnar, P., Anderson, R. S., Sue, C., & Delacou, B. (2007). Quaternary erosion-induced isostatic rebound in the western Alps. *Geology*, *35*(3), 195–198. https://doi.org/10.1130/G23053A.1

Champagnac, J.-D., Schlunegger, F., Norton, K., von Blanckenburg, F., Abbühl, L. M., & Schwab, M. (2009). Erosion-driven uplift of the modern Central Alps. *Tectonophysics*, *474*(1-2), 236–249. https://doi.org/10.1016/j.tecto.2009.02.024

Coward, M. P. (1983). Thrust tectonics, thin skinned or thick skinned, and the continuation of thrusts to deep in the crust. *Journal of Structural Geology*, *5*(2), 113–123. https://doi.org/10.1016/0191-8141(83)90037-8

De La Taille, C. (2015). *Evaluation de l'activité tectonique quaternaire des failles du Jura Méridional (France)*. Laboratoire ISTerre: Université de Grenoble Alpes.

Deichmann, N. (1992). Structural and rheological implications of lower-crustal earthquakes below northern Switzerland. *Physics of the Earth and Planetary Interiors*, *69*(3-4), 270–280. https://doi.org/10.1016/0031-9201(92)90146-M

Deichmann, N., Baer, M., Braunmiller, J., Husen, S., Faeh, D., Giardini, D., et al. (2006). Earthquakes in Switzerland and surrounding regions during 2005. *Eclogae Geologicae Helvetiae*, *99*(3), 443–452. https://doi.org/10.1007/s00015-006-1201-1

Deichmann, N., Clinton, J., Husen, S., Edwards, B., Haslinger, F., Fäh, D., et al. (2012). Earthquakes in Switzerland and surrounding regions during 2011. *Swiss Journal of Geosciences*, *105*(3), 463–476. https://doi.org/10.1007/s00015-012-0116-2

Delacou, B., Sue, C., Champagnac, J.-D., & Burkhard, M. (2004). Present-day geodynamics in the bend of the western and central Alps as constrained by earthquake analysis. *Geophysical Journal International*, *158*(2), 753–774. https://doi.org/10.1111/j.1365-246X.2004.02320.x

Delacou, B., Sue, C., Champagnac, J.-D., & Burkhard, M. (2005). Origin of the current stress field in the western/central Alps: Role of gravitational re-equilibration constrained by numerical modelling. *Geological Society of London, Special Publication*, *243*(1), 295–310. https://doi.org/10.1144/GSL.SP.2005.243.01.19

Delacou, B., Sue, C., Nocquet, J.-M., Champagnac, J.-D., Allanic, C., & Burkhard, M. (2008). Quantification of strain rate in the Western Alps using geodesy: Comparisons with seismotectonics. *Swiss Journal of Geosciences*, *101*(2), 377–385. https://doi.org/10.1007/s00015-008-1271-3

Delvaux, D. (1993). The TENSOR program for paleostress reconstruction: Examples from the east African and the Baikal rift zones. *Terra Nova*, *5*, 216.

Dèzes, P., Schmid, S. M., & Ziegler, P. A. (2004). Evolution of the European Cenozoic Rift System: Interaction of the Alpine and Pyrenean orogens with their foreland lithosphere. *Tectonophysics*, *389*(1-2), 1–33. https://doi.org/10.1016/j.tecto.2004.06.011

Gephart, J. W. (1990). Stress and the direction of slip on fault planes. *Tectonics*, *9*, 845–858. https://doi.org/10.1029/TC009i004p00845

Giamboni, M., Ustaszewski, K., Schmid, S. M., Schumacher, M. E., & Wetzel, A. (2004). Plio-Pleistocene transpressional reactivation of Paleozoic and Paleogene structures in the Rhine-Bresse transform zone (northern Switzerland and eastern France). *International Journal of Earth Sciences*, *93*(2), 207–223. https://doi.org/10.1007/s00531-003-0375-2

Giamboni, M., Wetzel, A., Nivière, B., & Schumacher, M. (2004). Plio-Pleistocene folding in the southern Rhinegraben recorded by the evolution of the drainage network (Sundgau area; northwestern Switzerland and France). *Eclogae Geologicae Helvetiae*, *97*(1), 17–31. https://doi.org/10.1007/s00015-004-1112-4

Gutenberg, B., & Richter, C. F. (1942). Earthquake magnitude, intensity, energy, and acceleration. *Bulletin of the Seismological Society of America*, *32*, 163–191.

Gutenberg, B., & Richter, C. F. (1956). Magnitude and energy of earthquakes. *Annales de Geophysique*, *9*, 1–15.
Hardebeck, J. L., & Michael, A. J. (2006). Damped regional-scale stress inversions: Methodology and examples for southern California and the Coalinga aftershock sequence. *Journal of Geophysical Research*, *111*, B11310. https://doi.org/10.1029/2005JB004144
Heim, A., 1919. Geologie der Schweiz.
Henry, P., Deloule, E., & Michard, A. (1997). The erosion of the Alps: Nd isotopic and geochemical constraints on the sources of the peri-alpine molasse sediments. *Earth and Planetary Science Letters*, *146*(3-4), 627–644. https://doi.org/10.1016/S0012-821X(96)00252-X
Herring, T.A., King, R.W., McClusky, S.C., 2010. Introduction to GAMIT/GLOBK. Release 10.4. Boston: Department of Earth, Atmospheric, and Planetary Sciences. MIT.(2010-10-04)[2013-05-15]. http://www-gpsg.mit.edu/-simon/gtgk/Intro_GG.pdf
Hindle, D., 1997. Quantifying stresses and strains from the Jura Arc, and their usefulness in choosing a deformation model for the region. Neuchatel.
Homberg, C., Hu, J. C., Angelier, J., Bergerat, F., & Lacombe, O. (1997). Characterization of stress perturbations near major fault zones: Insights from 2-D distinct-element numerical modelling and field studies (Jura Mountains). *Journal of Structural Geology*, *19*(5), 703–718. https://doi.org/10.1016/S0191-8141(96)00104-6
Homberg, C., Lacombe, O., Angelier, J., & Bergerat, F. (1999). New constraints for indentation mechanisms in arcuate belts from the Jura Mountains, France. *Geology*, *27*(9), 827–830. https://doi.org/10.1130/0091-7613(1999)027<0827:NCFIMI>2.3.CO;2
Homberg, C., Bergerat, F., Philippe, Y., Lacombe, O., & Angelier, J. (2002). Structural inheritance and Cenozoic stress fields in the Jura fold-and-thrust belt (France). *Tectonophysics, Paleostresses and Tectonics in the Peri-Tethyan Margins*, *357*, 137–158. https://doi.org/10.1016/S0040-1951(02)00366-9
Illies, J. H., & Greiner, G. (1978). Rhinegraben and the Alpine system. *Geological Society of America Bulletin*, *89*(5), 770–782. https://doi.org/10.1130/0016-7606(1978)89<770:RATAS>2.0.CO;2
Jouanne, F., Menard, G., & Darmendrail, X. (1995). Present-day vertical displacements in the north-western Alps and southern Jura Mountains—Data from leveling comparisons. *Tectonics*, *14*, 606–616. https://doi.org/10.1029/94TC03336
Jouanne, F., Genaudeau, N., Menard, G., & Darmendrail, X. (1998). Estimating present-day displacement fields and tectonic deformation in active mountain belts: An example from the Chartreuse Massif and the southern Jura Mountains, western Alps. *Tectonophysics*, *296*(3-4), 403–419. https://doi.org/10.1016/S0040-1951(98)00156-5
Kastrup, U., Zoback, M. L., Deichmann, N., Evans, K. F., Giardini, D., & Michael, A. J. (2004). Stress field variations in the Swiss Alps and the northern Alpine foreland derived from inversion of fault plane solutions. *Journal of Geophysical Research*, *109*, B01402. https://doi.org/10.1029/2003JB002550
Lacombe, O. (2012). Do fault slip data inversions actually yield "paleostresses" that can be compared with contemporary stresses? A critical discussion. *Comptes Rendus Geosci., Tectonophysics in Russia and France: A project initiated by Jacques Angelier/La tectonophsique en Russie et en France: Un projet initié par Jacques Angelier*, *344*(3-4), 159–173. https://doi.org/10.1016/j.crte.2012.01.006
Lacombe, O., & Mouthereau, F. (2002). Basement-involved shortening and deep detachment tectonics in forelands of orogens: Insights from recent collision belts (Taiwan, Western Alps, Pyrenees). *Tectonics*, *21*(4), 1030. https://doi.org/10.1029/2001TC901018
Lacombe, O., Angelier, J., Byrne, D., & Dupin, J. M. (1993). Eocene-Oligocene tectonics and kinematics of the Rhine-Saone Continental Transform Zone (eastern France). *Tectonics*, *12*, 874–888. https://doi.org/10.1029/93TC00233
Laubscher, H. (1992). Jura kinematics and the Molasse Basin. *Eclogae Geologicae Helvetiae*, *85*, 653–675.
Laubscher, H. (2010). Jura, Alps and the boundary of the Adria subplate. *Tectonophysics*, *483*(3-4), 223–239. https://doi.org/10.1016/j.tecto.2009.10.011
Lebeau, R. (1951). Sur la structure du Jura: les enseignements de l'excursion géologique interuniversitaire en Franche-Comté (31 août - 6 septembre 1949). *Revue de géographie de Lyon*, *26*(1), 71–75. https://doi.org/10.3406/geoca.1951.6039
Lund, B., & Townend, J. (2007). Calculating horizontal stress orientations with full or partial knowledge of the tectonic stress tensor. *Geophysical Journal International*, *170*(3), 1328–1335. https://doi.org/10.1111/j.1365-246X.2007.03468.x
Lyard, F., Lefevre, F., Letellier, T., & Francis, O. (2006). Modelling the global ocean tides: Modern insights from FES2004. *Ocean Dynamics*, *56*(5-6), 394–415. https://doi.org/10.1007/s10236-006-0086-x
Lyon-Caen, H., & Molnar, P. (1989). Constraints on the deep structure and dynamic processes beneath the Alps and adjacent regions from an analysis of gravity anomalies. *Geophysical Journal International*, *99*(1), 19–32. https://doi.org/10.1111/j.1365-246X.1989.tb02013.x
Madritsch, H., Schmid, S. M., & Fabbri, O. (2008). Interactions between thin- and thick-skinned tectonics at the northwestern front of the Jura fold-and-thrust belt (eastern France). *Tectonics*, *27*, TC5005. https://doi.org/10.1029/2008TC002282
Madritsch, H., Kounov, A., Schmid, S. M., & Fabbri, O. (2009). Multiple fault reactivations within the intra-continental Rhine–Bresse Transfer Zone (La Serre Horst, eastern France). *Tectonophysics*, *471*(3-4), 297–318. https://doi.org/10.1016/j.tecto.2009.02.044
Madritsch, H., Fabbri, O., Hagedorn, E.-M., Preusser, F., Schmid, S. M., & Ziegler, P. A. (2010). Feedback between erosion and active deformation: Geomorphic constraints from the frontal Jura fold-and-thrust belt (eastern France). *International Journal of Earth Sciences*, *99*, S103–S122. https://doi.org/10.1007/s00531-009-0468-7
Madritsch, H., Preusser, F., Fabbri, O., Bichet, V., Schlunegger, F., & Schmid, S. M. (2010). Late Quaternary folding in the Jura Mountains: Evidence from syn-erosional deformation of fluvial meanders. *Terra Nova*, *22*(2), 147–154. https://doi.org/10.1111/j.1365-3121.2010.00928.x
Martínez-Garzón, P., Kwiatek, G., Ickrath, M., & Bohnhoff, M. (2014). MSATSI: A MATLAB package for stress inversion combining solid classic methodology, a new simplified user-handling, and a visualization tool. *Seismological Research Letters*, *85*(4), 896–904. https://doi.org/10.1785/0220130189
Maury, J., Cornet, F. H., & Dorbath, L. (2013). A review of methods for determining stress fields from earthquakes focal mechanisms; Application to the Sierentz 1980 seismic crisis (Upper Rhine graben). *Bulletin de la Societe Geologique de France*, *184*(4-5), 319–334. https://doi.org/10.2113/gssgfbull.184.4-5.319
Merle, O., & Michon, L. (2001). The formation of the West European rift; A new model as exemplified by the Massif Central area. *Bulletin de la Societe Geologique de France*, *172*(2), 213–221. https://doi.org/10.2113/172.2.213
Michael, A. J. (1984). Determination of stress from slip data: Faults and folds. *Journal of Geophysical Research*, *89*, 11,517–11,526. https://doi.org/10.1029/JB089iB13p11517
Michael, A. J. (1987). Use of focal mechanisms to determine stress: A control study. *Journal of Geophysical Research*, *92*, 357–368. https://doi.org/10.1029/JB092iB01p00357
Michael, A. J. (1991). Spatial variations in stress within the 1987 Whittier Narrows, California, aftershock sequence: New techniques and results. *Journal of Geophysical Research*, *96*, 6303–6319. https://doi.org/10.1029/91JB00195
Molliex, S., Fabbri, O., Bichet, V., & Madritsch, H. (2011). Possible Quaternary growth of a hidden anticline at the front of the Jura fold-and-thrust belt: Geomorphological constraints from the Foret de Chaux area, France. *Bulletin de la Societe Geologique de France*, *182*(4), 337–346. https://doi.org/10.2113/gssgfbull.182.4.337

Nivière, B., & Winter, T. (2000). Pleistocene northwards fold propagation of the Jura within the southern upper Rhine graben: Seismotectonic implications. *Global and Planetary Change*, *27*(1-4), 263–288. https://doi.org/10.1016/S0921-8181(01)00070-4

Nivière, B., Giamboni, M., Innocent, C., & Winter, T. (2006). Kinematic evolution of a tectonic wedge above a flat-lying décollement: The Alpine Foreland at the interface between the Jura Mountains (northern Alps) and the upper Rhine graben. *Geology*, *34*(6), 469–472. https://doi.org/10.1130/G22334.1

Nocquet, J.-M. (2012). Present-day kinematics of the Mediterranean: A comprehensive overview of GPS results. *Tectonophysics, Orogenic processes and structural heritage in Alpine-type mountain belts*, *579*, 220–242. https://doi.org/10.1016/j.tecto.2012.03.037

Nocquet, J.-M., & Calais, E. (2003). Crustal velocity field of western Europe from permanent GPS array solutions, 1996–2001. *Geophysical Journal International*, *154*(1), 72–88. https://doi.org/10.1046/j.1365-246X.2003.01935.x

Nocquet, J.-M., Sue, C., Walpersdorf, A., Tran, T., Lenôtre, N., Vernant, P., et al. (2016). Present-day uplift of the western Alps. *Scientific Reports*, *6*(1), 28404. https://doi.org/10.1038/srep28404

Pfiffner, O. A. (1990). Kinematics and intrabed-strain in mesoscopically folded limestone layers—Examples from the Jura and the helvetic zone of the Alps. *Eclogae Geologicae Helvetiae*, *83*, 585–602.

Plenefisch, T., & Bonjer, K.-P. (1997). The stress field in the Rhine graben area inferred from earthquake focal mechanisms and estimation of frictional parameters. *Tectonophysics*, *275*(1-3), 71–97. https://doi.org/10.1016/S0040-1951(97)00016-4

Rabin, M., Sue, C., Valla, P. G., Champagnac, J.-D., Carry, N., Bichet, V., et al. (2015). Deciphering neotectonics from river profile analysis in the karst Jura Mountains (northern Alpine Foreland). *Swiss Journal of Geosciences*, 1–24. https://doi.org/10.1007/s00015-015-0200-5

Reilinger, R., McClusky, S., Vernant, P., Lawrence, S., Ergintav, S., Cakmak, R., et al. (2006). GPS constraints on continental deformation in the Africa-Arabia-Eurasia continental collision zone and implications for the dynamics of plate interactions. *Journal of Geophysical Research*, *111*, B05411. https://doi.org/10.1029/2005JB004051

RESIF (2017). RESIF-RENAG French National Geodetic Network. *RESIF - Réseau Sismologique et géodésique Français*. https://doi.org/10.15778/resif.rg

Rollier, L. (1903). Le plissement de la chaine du Jura. *Annales de Géographie*, *12*(66), 403–410. https://doi.org/10.3406/geo.1903.6377

Rouland, D., Haessler, H., Bonjer, K.P., Gilg, B., Mayer-Rosa, D., Pavoni, N., 1980. The Sierentz southern-rhinegraben earthquake of July 15, 1980. Preliminary results. Proc. 17th Assem. ESC Bp. 441–446.

Schlunegger, F., Jordan, T. E., & Klaper, E. M. (1997). Controls of erosional denudation in the orogen on foreland basin evolution: The Oligocene central Swiss Molasse Basin as an example. *Tectonics*, *16*, 823–840. https://doi.org/10.1029/97TC01657

Serpelloni, E., Faccenna, C., Spada, G., Dong, D., & Williams, S. D. P. (2013). Vertical GPS ground motion rates in the Euro-Mediterranean region: New evidence of velocity gradients at different spatial scales along the Nubia-Eurasia plate boundary. *Journal of Geophysical Research: Solid Earth*, *118*, 6003–6024. https://doi.org/10.1002/2013JB010102

Sommaruga, A. (1999). Decollement tectonics in the Jura foreland fold-and-thrust belt. *Marine and Petroleum Geology*, *16*(2), 111–134. https://doi.org/10.1016/S0264-8172(98)00068-3

Sue, C., & Schmid, S. M. (2017). From ocean formation to mountain evolution in Alpine-type orogens. *Swiss Journal of Geosciences*, *110*(2), 417–418. https://doi.org/10.1007/s00015-017-0273-4

Sue, C., & Tricart, P. (2003). Neogene to ongoing normal faulting in the inner western Alps: A major evolution of the late Alpine tectonics. *Tectonics*, *22*(5), 1050. https://doi.org/10.1029/2002TC001426

Sue, C., Thouvenot, F., Frechet, J., & Tricart, P. (1999). Widespread extension in the core of the western Alps revealed by earthquake analysis. *Journal of Geophysical Research*, *104*, 25,611–25,622. https://doi.org/10.1029/1999JB900249

Sue, C., Grasso, J., Lahaie, F., & Amitrano, D. (2002). Mechanical behavior of western Alpine structures inferred from statistical analysis of seismicity. *Geophysical Research Letters*, *29*(8), 1224. https://doi.org/10.1029/2001GL014050

Sue, C., Delacou, B., Champagnac, J.-D., Allanic, C., Tricart, P., & Burkhard, M. (2007). Extensional neotectonics around the bend of the Western/Central Alps: An overview. *International Journal of Earth Sciences*, *96*(6), 1101–1129. https://doi.org/10.1007/s00531-007-0181-3

Thouvenot, F., Frechet, J., Tapponnier, P., Thomas, J. C., Le Brun, B., Menard, G., et al. (1998). The M-L 5.3 Epagny (French Alps) earthquake of 1996 July 15: A long-awaited event on the Vuache fault. *Geophysical Journal International*, *135*(3), 876–892. https://doi.org/10.1046/j.1365-246X.1998.00662.x

Tricart, P., Lardeaux, J.-M., Schwartz, S., & Sue, C. (2006). The late extension in the inner western Alps: A synthesis along the south-Pelvoux transect. *Bulletin de la Societe Geologique de France*, *177*(6), 299–310. https://doi.org/10.2113/gssgfbull.177.6.299

Twiss, R. J., & Unruh, J. R. (1998). Analysis of fault slip inversions: Do they constrain stress or strain rate? *Journal of Geophysical Research*, *103*, 12,205–12,222. https://doi.org/10.1029/98JB00612

Ustaszewski, K., & Schmid, S. M. (2006). Control of preexisting faults on geometry and kinematics in the northernmost part of the Jura fold-and-thrust belt. *Tectonics*, *25*, TC5003. https://doi.org/10.1029/2005TC001915

Ustaszewski, K., & Schmid, S. M. (2007). Latest Pliocene to recent thick-skinned tectonics at the upper Rhine graben–Jura Mountains junction. *Swiss Journal of Geosciences*, *100*(2), 293–312. https://doi.org/10.1007/s00015-007-1226-0

Valla, P. G., van der Beek, P. A., Shuster, D. L., Braun, J., Herman, F., Tassan-Got, L., & Gautheron, C. (2012). Late Neogene exhumation and relief development of the Aar and Aiguilles Rouges massifs (Swiss Alps) from low-temperature thermochronology modeling and $^{4}He/^{3}He$ thermochronometry. *Journal of Geophysical Research*, *117*, F01004. https://doi.org/10.1029/2011JF002043

Vernant, P., Hivert, F., Chéry, J., Steer, P., Cattin, R., & Rigo, A. (2013). Erosion-induced isostatic rebound triggers extension in low convergent mountain ranges. *Geology*, *41*(4), 467–470. https://doi.org/10.1130/G33942.1

Vouillamoz, N. (2015). *Microseismic characterization of Fribourg area (Switzerland) by nanoseismic monitoring*. Department of Geoscience: Fribourg.

Wallace, R. E. (1951). Geometry of shearing stress and relation to faulting. *Journal of Geology*, *59*(2), 118–130. https://doi.org/10.1086/625831

Walpersdorf, A., Baize, S., Calais, E., Tregoning, P., & Nocquet, J.-M. (2006). Deformation in the Jura Mountains (France): First results from semi-permanent GPS measurements. *Earth and Planetary Science Letters*, *245*(1-2), 365–372. https://doi.org/10.1016/j.epsl.2006.02.037

Walpersdorf, A., Pinget, L., Vernant, P., Sue, C., Deprez, A., & the RENAG team (2018). Does long-term GPS in the Western Alps finally confirm earthquake mechanisms? *Tectonics*, *37*. https://doi.org/10.1029/2018TC005054

Yamaji, A. (2000). The multiple inverse method: A new technique to separate stresses from heterogeneous fault-slip data. *Journal of Structural Geology*, *22*(4), 441–452. https://doi.org/10.1016/S0191-8141(99)00163-7

Yamaji, A. (2003). Are the solutions of stress inversion correct? Visualization of their reliability and the separation of stresses from heterogeneous fault-slip data. *Journal of Structural Geology*, *25*(2), 241–252. https://doi.org/10.1016/S0191-8141(02)00021-4

Yamaji, A., & Sato, K. (2006). Distances for the solutions of stress tensor inversion in relation to misfit angles that accompany the solutions. *Geophysical Journal International*, *167*(2), 933–942. https://doi.org/10.1111/j.1365-246X.2006.03188.x

Zoback, M., 1992. First- and second-order patterns of stress in the lithosphere: The world stress map project. USGS Staff-Publ. Res.